Geogrid-anchored sheet pile walls
a small-scale experimental and numerical study

Wittekoek, B.; Van Eekelen, S. J.M.; Terwindt, J.; Korff, M.; Van Duijnen, P. G.; Detert, O.; Bezuijen, A.

DOI
10.1680/jgein.22.00501

Publication date
2022

Document Version
Final published version

Published in
Geosynthetics International

Geogrid-anchored sheet pile walls; a small-scale experimental and numerical study

B. Wittekoek[1], S. J. M. van Eekelen[2], J. Terwindt[3], M. Korff[4], P. G. van Duijnen[5], O. Detert[6] and A. Bezuijen[7]

[1]*Geotechnical researcher and adviser at Deltares, Geo-engineering Department, Delft, Netherlands, E-mail: britt.wittekoek@deltares.nl*
[2]*Geotechnical researcher and expert adviser at Deltares, Geo-engineering Department, Delft, Netherlands, E-mail: suzanne.vaneekelen@deltares.nl (corresponding author)*
[3]*Data Engineer at Scarp DENA, former Technician at Deltares, Geo-engineering Department, Delft, Netherlands, E-mail: jarno.terwindt@gmail.com*
[4]*Geotechnical senior adviser and Innovations Manager at Deltares, Geo-engineering Department, Delft, Netherlands, E-mail: mandy.korff@deltares.nl; Associate Professor in Geotechnical Practice at Delft University of Technology, Faculty of Civil Engineering and Geosciences, Delft, Netherlands, E-mail: m.korff@tudelft.nl*
[5]*Geotechnical expert at Geotec Solutions, Culemborg, Netherlands, E-mail: pgvanduijnen@geotecsolutions.nl*
[6]*Head of Engineering Department, Huesker GmbH, Gescher, Germany, E-mail: detert@huesker.de*
[7]*Professor - Emeritus at Ghent University, Faculty of Engineering and Architecture, Department of Civil Engineering, Ghent, Belgium, E-mail: adam.bezuijen@ugent.be; Geotechnical expert, Deltares, Netherlands*

Received 24 March 2021, accepted 23 March 2022

ABSTRACT: The use of geogrids to anchor Sheet Pile Walls (SPW) is relatively new. A series of small-scale tests was performed to investigate the behaviour of geogrid-anchored SPWs subjected to strip footing surcharge loading. Particle Image Velocimetry (PIV) techniques were used to measure soil displacement and analyse the global failure mechanism and dominant soil-geogrid interaction mechanisms. One of the tests was duplicated in a test box that was eight times as wide, showing that the influence of the small width of the test box was acceptably small. A 2D finite element model (PLAXIS) was used to simulate the tests and there was a reasonable match with the test results. The position of the strip footing load, and the length and number of the geogrid anchors, proved to be key factors in determining the bearing capacity. The results provide new insights into the stabilising effect and the effective length of the geogrid anchors, in other words the length along which geogrid-soil friction is mobilised. Contrary to the Dutch design guidelines for reinforced soil walls and conventionally anchored sheet pile walls, the results showed that the geogrid provides resistance in the active zone under the strip footing surcharge loading.

KEYWORDS: Geosynthetics, sheet pile walls, anchorage, physical models, numerical analysis

REFERENCE: Wittekoek, B., van Eekelen, S. J. M., Terwindt, J., Korff, M., van Duijnen, P. G., Detert, O. and Bezuijen, A. (2022). Geogrid-anchored sheet pile walls; a small-scale experimental and numerical study. *Geosynthetics International*. [https://doi.org/10.1680/jgein.22.00501]

1. INTRODUCTION

Back-anchoring is a common and economical way of optimising the design of sheet pile walls. Steel and grout anchors have been widely applied for this purpose. The use of geogrids for the anchorage of SPWs, however, is a relatively new application. In this approach, SPWs can be anchored with one or more geogrid layers (Figure 1). This type of SPW anchorage has benefits such as the possibility of prestressing the anchorage earlier during the backfilling stage, reducing horizontal deformation as a result. In addition, it is also possible to anchor the SPW continuously at several levels, making the design economic and allowing for the installation of piles through the geogrid anchors, providing greater project flexibility. The drawback of geogrid-anchored SPWs is that a relatively large amount of space is needed for the installation of the geogrids. Furthermore, the method is suitable for

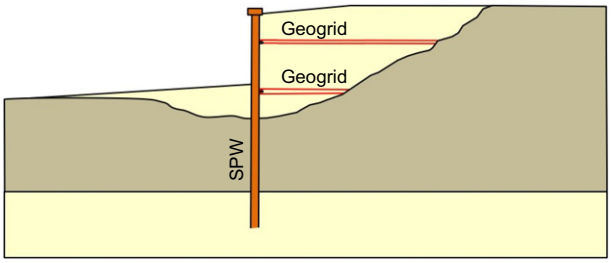

Figure 1. A geogrid-anchored sheet pile wall

backfilling projects only and not for building pits with excavations.

Geogrid-anchored SPWs have already been applied in several trial projects. Detert *et al*. (2019) describe several examples, including the widening of a railway, a motorway and a bridge abutment. van Duijnen *et al*. (2022) and Spingher (2018) describe the analysis of the construction of geogrid-anchored SPWs for wind-turbine peninsulas in Krammer, the Netherlands. The piles for these wind turbines were installed through the geogrid anchors. Twice the required anchor strength was applied to compensate for the loss of geogrid capacity due to the pile installation.

There is currently no accepted design method for geogrid-anchored SPWs. The construction method is comparable to both reinforced soil-retaining walls with a full-height rigid facing and traditionally anchored SPWs. The difference with the reinforced-soil approach is that the facing or the SPW is embedded in the ground. The SPW, for example, gives a higher bearing capacity for pile driving equipment that installs piles through the geogrid-anchorage, close the wall. Due to this advantage, several projects are in preparation in the Netherlands to apply geogrid-anchored SPWs. The difference with the approach using SPWs with traditional anchors is the amount of anchorage: a geogrid-anchored SPW can be anchored at several levels and along the full width. Furthermore, the geogrid anchor can behave differently as it can develop friction along its full length, and it may affect the shape and location of slip surfaces as well as the soil pressure exerted on the SPW. Extensive analytical and numerical calculations are therefore generally performed to design geogrid-anchored SPWs, with the most conservative results then being used.

The literature on geogrid-anchored SPWs is very limited. The scarce papers have been referred to above. Most of the closely related literature and design guidelines address geosynthetic-reinforced retaining walls (in the US: mechanically stabilized earth walls (MSE walls)) in combination with stiff facings, or SPWs with conventional grout anchors, see for example Bathurst *et al*. (2008) and Ahmadi (2020).

The design approach with reinforced soil considers external stability for the purposes of determining the required reinforcement length and embedding. The structure is checked for sliding, tilting and deep slip surfaces. Most design methods then check internal stability to determine the strength of the reinforcement and its connection with the facing if applicable, and the distance between the different layers (BS8006 2010; EBGEO 2010; CUR198 2017; Schaefer *et al*. 2017).

The design of conventionally anchored SPWs assumes that the anchors are effective only in the zone behind the active wedge that develops when the soil in front of the wall is excavated.

This paper presents part of a research programme that focuses on geogrid-anchored SPWs under strip footing loading. The aim of the programme is to investigate the mechanisms that play a role in structures of this kind to identify the parallels and differences with conventionally anchored SPWs and geosynthetic-reinforced retaining walls. The ultimate goal is to add a section for the design of geogrid-anchored SPWs to the Dutch design guideline for SPWs. The research programme includes trial projects (Detert *et al*. 2019), field monitoring (Spingher 2018; van Duijnen *et al*. 2022), small-scale laboratory tests with numerical simulations (Wittekoek 2020 and this paper). Medium-scale tests, centrifuge tests and more field monitoring are expected at a later stage.

This paper reports on a series of small-scale tests and 2D numerical simulations for one of those tests. Wittekoek (2020) gives more detailed information on the tests and numerical analysis. The analyses of these tests and numerical analyses are a first step towards a better understanding of the behaviour of this type of SPW anchorage and to determining the differences with conventionally anchored SPWs and geosynthetic-reinforced retaining walls.

2. SMALL-SCALE TESTS

2.1. Test set-up

A series of small-scale tests were performed in the Deltares laboratory in Delft, the Netherlands. The choice of a relatively small model and modelling at single gravity (1$\boldsymbol{g}$) made it possible to conduct a large number of tests economically. The model was a 1 : 16 scaled and simplified version of one of the SPWs installed in Windpark Krammer (van Duijnen *et al*. 2022). The tests were conducted to investigate failure mechanisms for different configurations and to investigate to what extent these failure mechanisms can be simulated numerically. This section describes the tests, test set-up and materials.

A sand body and a small geogrid-anchored SPW were installed in a transparent test box ($L \times B \times H =$ $525 \times 100 \times 300$ mm) as shown in Figure 2. A 0.10-m-long strip footing surcharge load was applied behind the SPW using a barrel that was filled with water with a constant flow rate during the test. This paper states the applied strip footing surcharge load in kN per m SPW (kN/m). The strip footing was 0.1 m wide and so an applied load of 1 kN/m corresponds to a surcharge load of 10 kPa. The constant flow rate ranged between 0.02 and 0.03 kg/s. The barrel could only move vertically and rested on two stiff footing plates (0.10 m $\times$ 0.09 m) with a rod in between. This structure allows the footing to follow the vertical and horizontal movements of the soil freely.

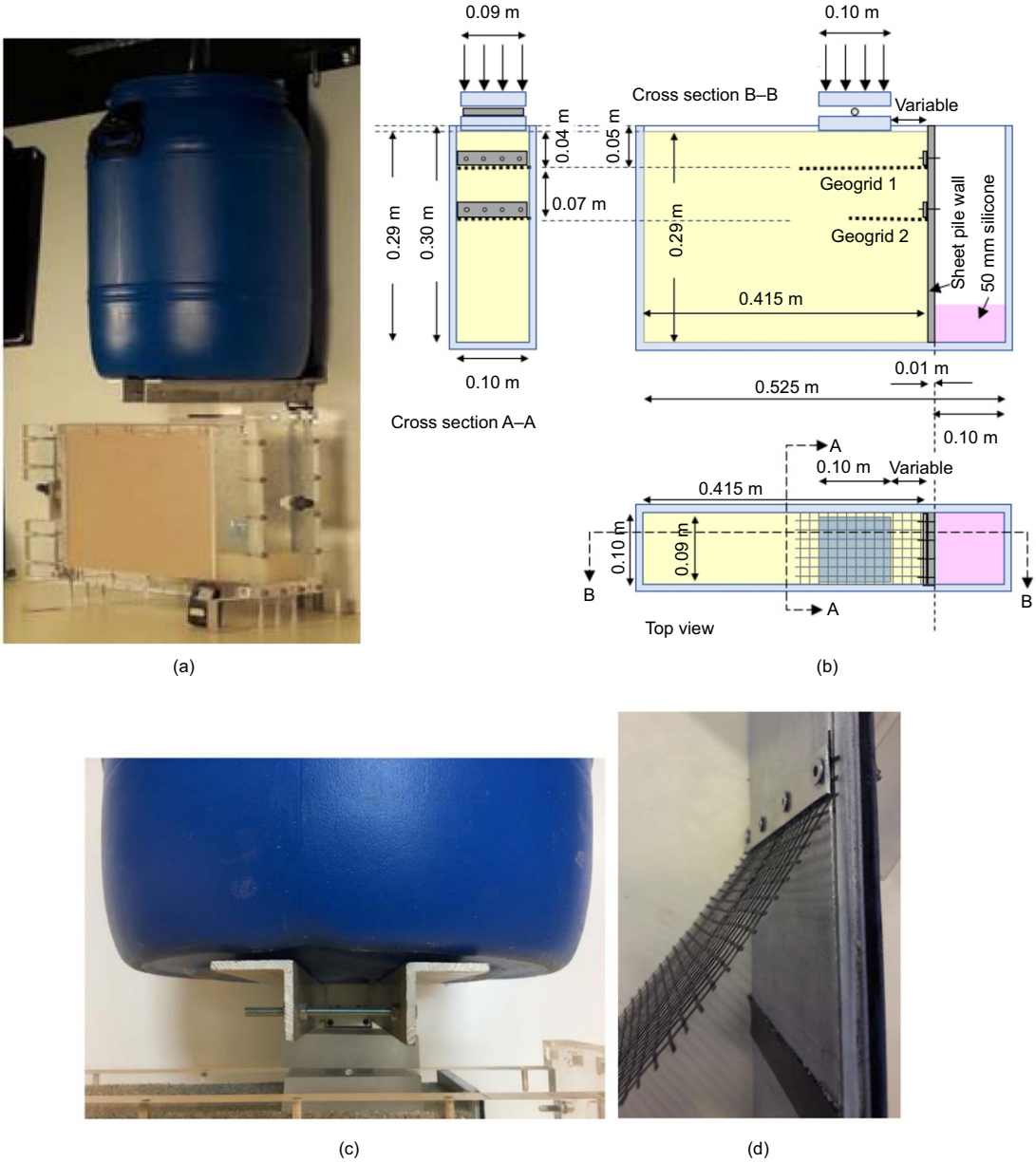

Figure 2. Test set-up (a) overview; (b) top view and cross-sections; (c) strip footing surcharge load; (d) geogrid-SPW connection

A 10-mm-thick aluminium plate modelled the SPW. Only the upper part of the embedded part of the SPW was modelled in order to keep the geometrical scaling factor limited. The shortened sheet pile wall was therefore free to slide along the box bottom. The sides of the SPW were covered with a sealing strip to keep the sand in. The bending stiffness of the SPW was chosen as the lead parameter for determining the thickness of the SPW. If the soil stresses were the same in the prototype and the scale model, the bending stiffness of the SPW, assumed to be a plane-strain structure, would scale with the geometrical scale $N^3 = 16^3$. However, the soil stresses are not the same. The scaling factor for the stress halfway the height of the SPW is approximately 2, resulting in a scaling factor for the secant Young's modulus soil stiffness of $2^{0.54} = 1.45$, where $m = 0.54$ was determined with triaxial tests. The bending stiffness of the prototype SPW (AZ13-700) is 43 000 kNm^2/m, the target stiffness of the model-SPW is 43 000/16^3/1.45 = 7.3 kNm^2/m (Iai 1989), which is a good match with the model-SPW stiffness of 5.8 kNm^2/m. Therefore, the stiffness of the model-SPW is accurate.

The SPW was anchored with either one or two geogrids. The scaled geogrids consisted of coated polypropylene yarns. The grid structure was formed by intertwining the transverse and longitudinal bundles of fibres. The thickness of the transverse ribs was approximately 0.3 mm and the aperture size was approximately 3 to 4 mm. The tensile stiffness and tensile strength properties were derived from tensile tests (following DIN EN ISO 2015) and they depend on the exhibit time and strain level (Bathurst and Naftchali 2021). The short-term stiffness at 2% axial strain was 191 kN/m and the tensile strength was 16.18 kN/m at a maximum strain of 13.48%. This tensile stiffness of the prototype geogrid (2 layers geogrid per anchor, 1 month-stiffness at 1.5%) was 3280 kN/m. Following Iai (1989), this stiffness should be scaled with

the geometric scaling factor ($N = 16$) and the Young's modulus scaling factor that takes into account the soil pressure underneath the surcharge load. The Young's modulus scaling factor is determined as $1.6^m = 1.3$, where the soil pressure prototype/model = 1.6 and the value of power m was given above. Scaling the prototype geogrid stiffness to model geogrid stiffness therefore gives 3280/16/1.3 = 159 kN/m. The applied model geogrid of 191 kN/m is sufficiently close to the desired model stiffness of 159 kN/m.

The geogrid was clamped underneath an aluminium strip that was screwed onto the SPW, as shown in Figure 2d. When two geogrids were applied, the vertical distance between the geogrids was 70 mm. With the geometric scaling factor $N = 16$, this corresponds to a prototype geogrid spacing of 16×0.07 m = 1.12 m. This is a realistic distance. For example, a geogrid distance of 1.20 m was applied in the Krammer wind-turbine project (Spingher 2018; van Duijnen *et al.* 2022).

Lees (2014) conducted direct shear experiments on a fill of diabase stone with a D_{50} of 5 mm. He found an influence zone around a Tensar TX160 geogrid of 0.30 m. The current model sand has a D_{50} of 0.14 mm. This is 35 times smaller than the D_{50} in the tests conducted by Lees (2014). The influence zone might therefore scale with 1 : 35 = 0.30 m / 35 = 9 mm. Furthermore, Ahmadi (2020) performed scaled tests of geosynthetic reinforced walls using a backfill sand with a D_{50} of 1.5 mm. The results of those tests showed that the horizontal deformation around the geogrids was localised to approximately 10 grains. We conclude from these studies that the two geogrids do not interfere in either the full-scale case of the Krammer project or the model tests described in this paper.

Baskarp B15 sand was used as the backfill material. This is a poorly graded sand with a median particle diameter (D_{50}) of 0.137 mm. The sand was densified to a relative density of ~70%. Table 1 lists the properties of the sand. The strength (mobilised internal friction angle φ) was derived from drained consolidated triaxial tests on samples with a similar density as in the tests, and at vertical strains similar to those found in the tests (~0.5 to 1.8%).

The passive soil side was modelled with a silicone block. A uniaxial compression test was conducted to determine linear-elastic behaviour and a stiffness of 159 kPa up to a strain level of at least 8%, which corresponds to 8 mm.

A Canon EOS 750D camera with a resolution of 24 megapixels (6000 × 4000) was positioned on a tripod approximately 1 m in front of the test box. The movement of the soil and SPW was tracked using one digital photograph every five seconds and the digital Particle Image Velocimetry (PIV) technique. PIV is a well-known technique that has been used by many researchers, including Dijkstra *et al.* (2008), Ahmadi and Hajialilue-Bonab (2012), Rui *et al.* (2016) and Ahmadi (2020). Different PIV programs are available. GeoPIV-RG (Stanier *et al.* 2015) is widely used and it has been validated by for example Stanier *et al.* (2016a, 2016b) and Teng *et al.* (2017). The agreement between GeoPIV-RG and manually tracked deformation was also checked in this study and it was found to be very good. GeoPIV-RG was therefore chosen for the analysis of soil deformation in the tests.

The passive soil was modelled with a silicone block that was less stiff than sand. The limited space behind the SPW in the small-test box would have led to excessively stiff behaviour if soil was used.

Table 1. Soil properties

Parameter	Symbol	Value
Relative density (%)	I_D	63–83
Median particle diameter (mm)	D_{50}	0.137
Coefficient of uniformity (–)	D_{60}/D_{10}	1.6
Secant internal friction angle (°)	φ_{sec}^{triax}	45[a]
Residual internal friction angle (°)	φ_{res}^{triax}	34
Dilatancy angle (°)	ψ^{triax}	15
Cohesion (kPa)	c	0.6
Secant Young's modulus at confining pressure of 100 kPa (MPa)	E_{50}^{ref}	72.4
Power in power law material stiffness[b] (–)	m	0.54
Poisson ratio (–)	v	0.25

[a]This value is a plane strain value and it was determined for triaxial tests with a relative density (59–93%), vertical strains (0.5–1.8%) and a stress level (20–60 kPa) similar to those in the tests. Accordingly, the triaxial value of $\varphi_{sec}^{triax} = 36.8°$ gives a plane strain value of (11/9) $\varphi_{sec}^{triax} = 45°$.

[b]$\frac{E_{50}}{E_{50,ref}} = \left(\frac{\sigma_3}{\sigma_{3,ref}}\right)^m$.

2.2. Testing procedure

The chronological order of the preparation phase was as follows: (1) lubricating the side walls and positioning of the silicone sheets, (2) placing the silicone block and SPW, horizontally restrained by a PVC plate which was clamped between the SPW and side wall, (3) simultaneous pouring and tamping of the sand up to the height of the geogrid anchor, (4) flattening the surface area before unfolding and placing the geogrid on top, (5) stretching the geogrid tight while pouring sand on top of it, (6) continuing until the sand was 10 mm below the top of the SPW and flattening out of the sand surface, (7) placing the bottom load plate (representing the strip footing), steel rod, second load plate and guidance rail on top of each other, and (8) placing the barrel on the guidance rail while a pipe was placed in the barrel and connected to the pump and the water reservoir.

The test started after the SPW support was removed. Just after the support was removed, the first photo of the series of test photos was taken, and the pump was switched on. The pump was switched off after the SPW failed by overturning or when the maximum allowable load of ~65 kg had been reached.

2.3. Boundary effects

The possible drawback of a narrow box is that the box walls have a relatively large effect on the test results. Two tests were conducted in a wider test box with the aim of obtaining more information about the influence of the width of the test box. The tests in the narrow box were

validated using the tests with the wider box (see Section 3.6).

The arching effect due to the back wall is considered negligible because the ratio of the spacing between the walls to the height of the wall is twice the ratio at which the back wall effect is less than 10% (Yang and Liu 2007). The friction between the SPW toe and box bottom and between the silicone block – box bottom was minimised by positioning a Teflon layer on the bottom and the SPW toe. The side-wall friction was minimised by lubricating the side walls with a low-friction water-based lubricant and positioning a highly adhesive silicone sheet on the side walls.

The total frictional force between the silicone sheet and side walls was measured separately in two ways: (1) by measuring the total vertical pressure at the bottom of the box. In this way, a reduction of ~33% in vertical pressure at the bottom of the box was measured, and (2) by measuring side-wall friction by lifting a bottomless box filled with sand. The side-wall friction angle was derived from the test results using Bathurst and Benjamin (1987) and Jewell (1987) and it was concluded that lubricating the side walls and covering them with silicone sheets reduced the side-wall friction angle from 16.2° to 11.0°.

Using a numerical approach, Jayasree *et al.* (2012) found a similar reduction in the horizontal, and therefore the vertical, soil pressures in their small-scale tests. For a width to height ratio of 0.4, they found a reduction in vertical soil pressures of 30% for dilative sand and a side-wall friction angle of 15°.

Three extension tests in line with Henkel and Gilbert (1952) showed that the average tensile stiffness of the 1 mm-thick silicone sheet was 300 kPa at a strain of 3%. The shear modulus of the backfill – derived from consolidated drained triaxial tests – is around ten times larger at the estimated horizontal soil pressures at which significant slipping of the soil body below the strip footing occurred. Correction of the bearing capacity for the resisting forces of the silicone sheet was therefore unnecessary.

2.4. Testing programme

Table 2 lists all the tests. The sand surface was 10 mm below the top of the SPW and the top geogrids were therefore installed 50 mm below the top of the SPW but 40 mm below the sand surface, as shown in Figure 2. The following parameters were varied:

- length of the geogrid: 60 mm, 110 mm, 130 mm or 180 mm;
- number of geogrids: one or two geogrids, or no geogrid;
- position of the load: 30 mm, 60 mm, 84 mm or 130 mm from the SPW;
- connection geogrid-SPW: connected or not connected to the SPW for all geogrid lengths tested.

3. RESULTS OF SMALL-SCALE TESTS

3.1. Introduction

This section describes the soil displacement that was observed and the development of slip surfaces. Sections 3.1–3.4 describe, in succession, the influence of: (1) the position of the strip footing surcharge load, (2) the length of the geogrid, (3) the addition of a second geogrid anchor and (4) the connection of the geogrid to the SPW. Section 3.5 includes an analysis of the reproducibility of the tests. Section 3.6 looks at the influence of the small test box width.

This section describes soil displacement for two points, Y and Z, respectively. These points are denoted by the red squares in the drawings at the bottom right of the figures.

Table 2. Overview of the small-scale tests

Test[a]	Number of geogrids; length of geogrid	Vertical distance geogrid (mm from top SPW)	Distance between load plate[b] and sheet pile wall (mm)	Relative density I_D (%)
Small-scale test box				
12/**13**	One; 110 mm	50	30	67/71
14/15	One; 110 mm	50	60	73/74
16/17/**45**	One; 180 mm	50	30	68/74/76
18/19	One; 180 mm	50	130	74/73
20/21	Two; 180 (top layer) and 110 mm	50 and 120	130	71/64
22/23	Two; 180 (top layer) and 110 mm	50 and 120	30	74/78
28	One; 60 mm	50	30	81
30	One; 60 mm	50	84	78
31	One; 60 mm; non-connected	50	30	68
41/**42**	One; 180 mm; non-connected	50	30	75/76
43/44	One; 110 mm; non-connected	50	30	69/76
47	No geogrid	—	84	75
48	No geogrid	—	30	71
51	One; 130 mm; non-connected	50	30	67
52	One; 130 mm	50	30	65
Wider medium-scale test box for validation of the small-width tests (see Section 3.6)				
5/6	One; 180 mm	50	30	71/70

[a]The results presented in this paper are the results of the tests with bold numbers. Similar results were produced by tests with a similar test configuration.
[b]The bottom load plate was 15 mm thick, 100 mm long (perpendicular to the SPW) and 90 mm wide (in-plane direction of digital test photos).

3.2. Location of strip footing surcharge load

Figure 3 shows the development of the slip surfaces for Test 19 with one 180 mm geogrid anchor. Figure 3a shows the full-field soil shear strain after two-thirds of the test (at a surcharge load of ~4 kN/m). The figure shows the general failure mechanism of a geogrid-anchored SPW subjected to a strip footing surcharge loading. It consists of two slip surfaces which develop from the inner and outer edge of the footing towards the SPW. The soil starts to slide along the critical slip surface (labelled 1A in the figure). A secondary slip surface – 1B – develops between the unstable soil mass, moving downwards and sideways due to the strip footing load, and the soil enclosed by the unstable soil mass and the SPW. Figure 3b shows how the soil domain behind the wall can be divided into three different strain zones: (I) a zone with rigid soil body motion between the wall and secondary slip surface, (II) an active zone below the strip footing enclosed by the secondary slip surface and the critical slip surface and (III) the stable soil zone behind the critical slip surface.

A third slip surface developed at large overturning values of the SPW, which occurred after the full development of the critical slip surface. As shown in Figure 3, this third slip surface developed at the outer edge of the strip footing at the ground surface level, like the critical slip surface, but intersected with the SPW at a shallower depth. This slip surface has been excluded from further analysis since this slip surface was seen in this specific test configuration only, and the SPW system was approaching a state of failure prior to the development of this slip surface.

Figure 4 shows how the load position affects soil displacement. Each graph shows the results for two tests with the same geogrid length. The soil response in the tests without anchorage (Figure 4a) was stiffer when the load was further away from the SPW. This is the result of the longer critical slip surface from the outer edge of the strip footing to the SPW: a longer slip surface mobilises more shear resistance. In addition, the larger distance between the load and the SPW gives a favourable (in other words, deeper) distribution of the load. Figure 4b shows the results of the tests with a 60 mm geogrid anchor. The load position of 84 mm from the SPW was chosen to ensure that the entire geogrid was located in zone I. Interestingly, the geogrids in these tests provided a significantly higher overall stability than in the situation without a geogrid (Figure 4a), even though the geogrids were located completely outside zones II and III.

Figures 4c and 4d show the results of the tests with the 110 mm and 180 mm geogrids.

All the graphs in Figure 4 show that the load position affects the vertical displacement: the closer the load to the SPW, the larger the vertical deformation for point Z. Note that in Figure 4c, the second load (Test 14) is very close to the SPW. This gives a significantly greater vertical displacement for point Z than the second load positions in the other graphs in Figure 4. The two loads in Figure 4c are the loads that are closest to each other, which is why the differences between the two load positions are the smallest in this graph.

Figure 4d shows that the anchorage is most effective when the vertical load on the geogrid is large. The SPW in Test 18 translates horizontally while, in Test 45, the SPW tilts backwards; the SPW toe translates more than the SPW head. This results in a different failure mechanism for the two load positions.

3.3. Length of the geogrid

Figure 5 shows the effect of the geogrid length on soil displacement. As expected, a positive relation was found between the failure load and geogrid length: the longer the geogrid, the higher the failure load and therefore the more resistance provided by the geogrid. The longest geogrid – 180 mm – responded more stiffly from the start of the test.

Figure 6a shows how geogrid length affects the critical slip surface. In the tests with a ≤130 mm geogrid anchor, a straight critical slip surface developed from the outer edge of the footing. With the 180 mm geogrid anchor, the same straight slip surface developed initially, as shown by the solid blue line. However, another slip surface became the critical one at final load level. With increasing displacement, the slip surface reoriented vertically at the

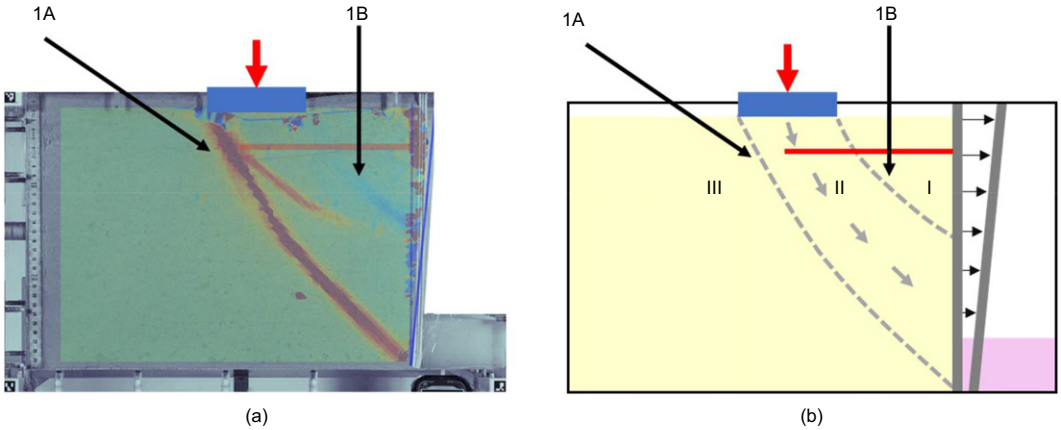

Figure 3. Slip surfaces: (a) soil shear strains for Test 19 with a 180 mm geogrid anchor and the load positioned 130 mm from the SPW; (b) schematisation of the general failure mechanism and the development of three different strain fields in the backfill behind the SPW

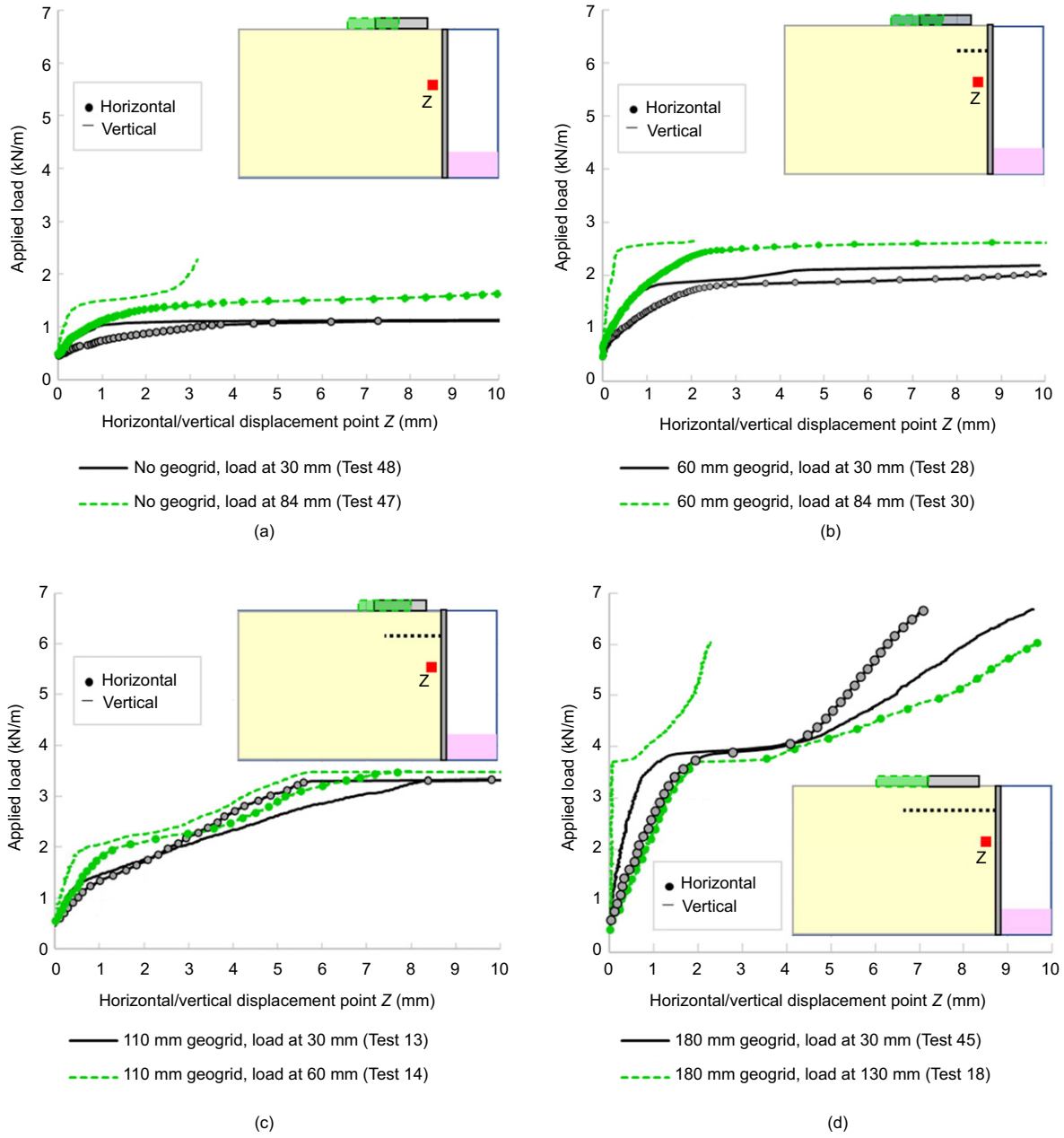

Figure 4. Effect of load position: relation between horizontal/vertical soil displacement and applied load for tests (a) without an anchor; (b) with a 60 mm geogrid anchor; (c) with a 110 mm geogrid anchor and (d) a 180 mm geogrid anchor

intersection with the geogrid. As a result, the straight slip surface changed into a slightly different curved critical slip surface.

Figure 6b shows the soil shear strains and the two slip surfaces for the 180 mm geogrid test. As can be seen, the length of the geogrid behind the slip surface in zone III is substantial in this case only. It is therefore assumed that the intersection with the slip surface activates the geogrid.

The slip surface follows the path of lowest resistance. The activation of the geogrid increases the soil shear strength locally and the increased shear strength of the soil in the vicinity of the geogrid therefore results in a vertical reorientation of the slip surface. This concurs with the results of the large-scale plane strain tests with geogrid reinforced soil from Ziegler (2010).

3.4. A second geogrid anchor

Figure 7 shows that adding a second geogrid reduces soil displacement at higher loads (≥4.0 kN/m). The top geogrid in this figure measures 180 mm, the second 110 mm. Up to an applied load of 3.0 kN/m, the soil response is similar in the tests with one and two geogrids. Between an applied load of 3.0 and 4.0 kN/m (=30–40 kPa), soil deformation is larger with two geogrids than with one. This can be ignored as it can be ascribed to the limited reproducibility for tests with large displacements of the SPW toe along the box bottom, as described in Section 3.5.

Figure 8 shows how a second geogrid affects the critical slip surface. Adding a second geogrid resulted in only a minor change to the critical slip surface, which became slightly wider and longer.

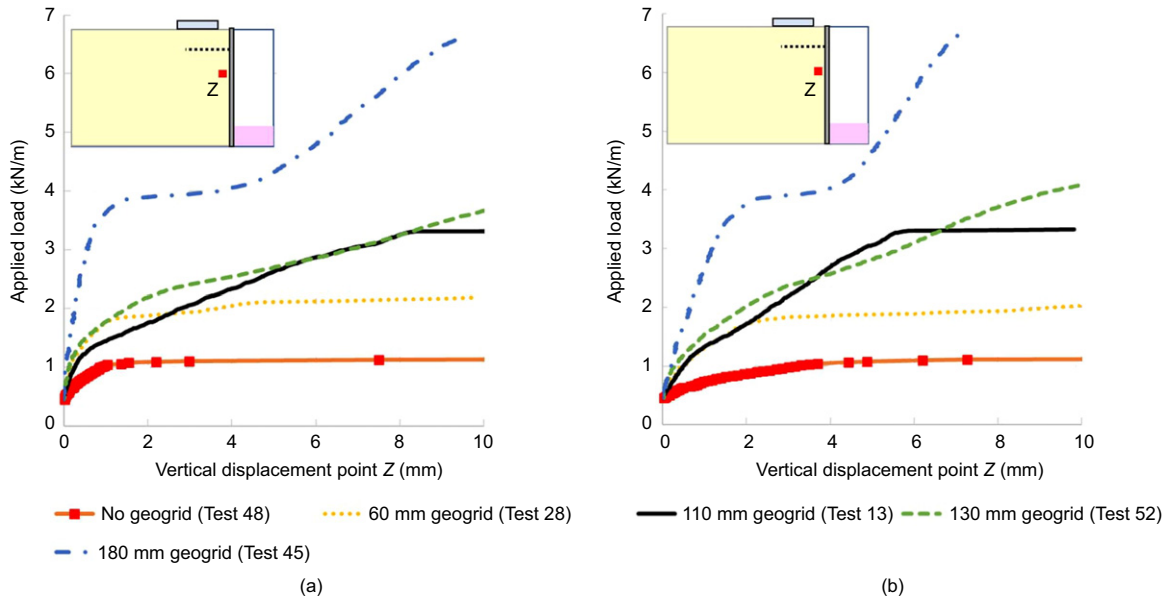

Figure 5. Effect of geogrid length: relation between horizontal/vertical soil displacement and applied load. Applied load at 30 mm from SPW

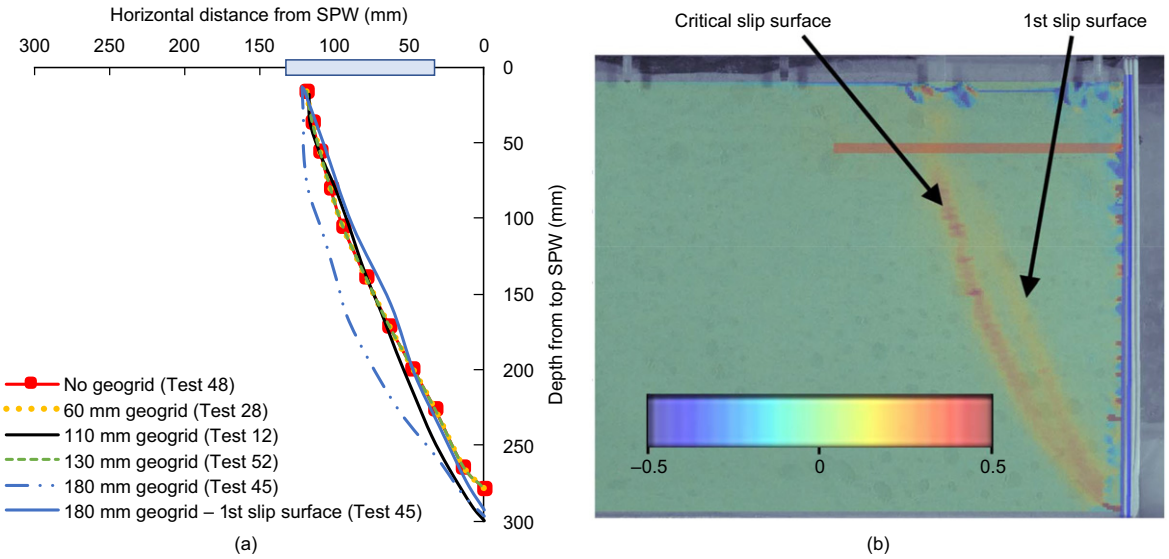

Figure 6. (a) Effect of geogrid length on the critical slip surfaces (b) shear strains (–) showing the 1st and critical slip surfaces for Test 45 with a 180 mm geogrid anchor. The load is positioned 30 mm from the SPW. The initial position of the geogrid in Test 45 is denoted in Figure (b) by the red line

3.5. Connection between geogrid and SPW

Figure 9 compares tests in which the geogrid is either connected or not connected to the SPW.

Figure 9 shows the following:

- Connecting a geogrid to the SPW results in a higher failure load than in the test without an anchor.
- Non-connected geogrids with a length ≤130 mm do not result in higher failure loads than in the test without an anchor. These relatively short geogrids are located in zones I and II, completely outside zone III. It can therefore be concluded that the confining effect for these short geogrids is very small or absent.
- Connected geogrids with a length ≤130 mm do provide resistance. Accordingly, zones I and II (Figure 3) are activated only when the geogrid is connected to the SPW. Vertical loads in zones I and II are transferred to the SPW via the geogrid. This mechanism is seen after some vertical displacement of the geogrid.
- The soil response in the test with a non-connected 180 mm geogrid was stiffer than in the test without a geogrid. The 180 mm geogrid evidently provided resistance, even though it was not connected to the SPW. Accordingly, the membrane effect contributes to the total bearing capacity for geogrids with a length beyond the active zone. Pull-out resistance is provided

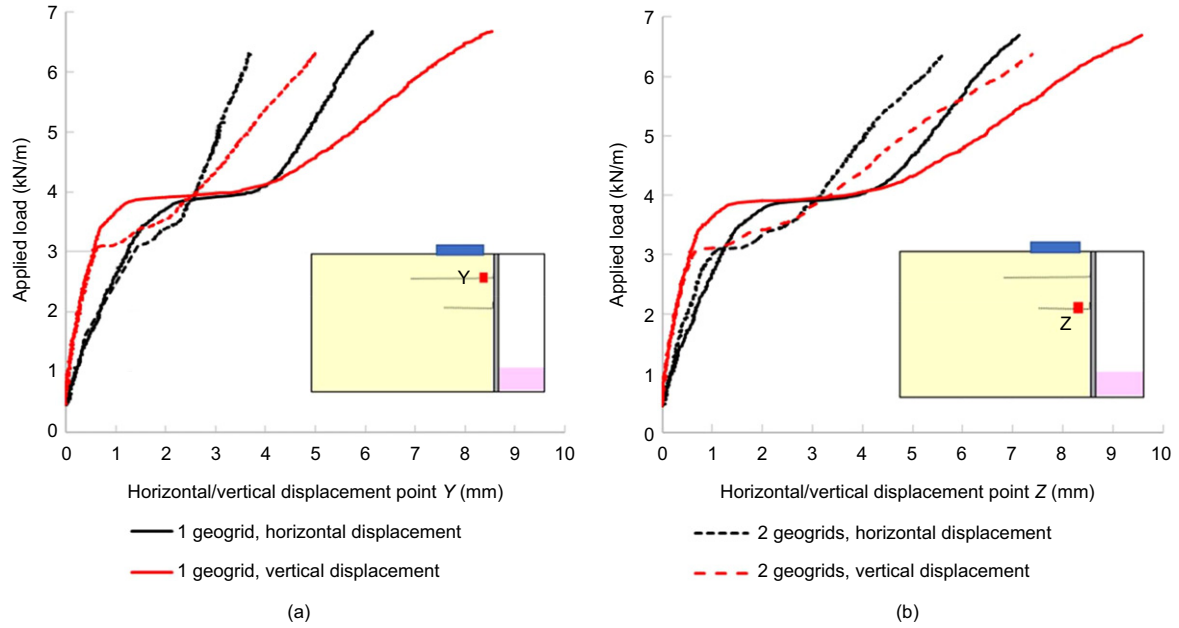

Figure 7. Effect of a second geogrid: relation between horizontal and vertical soil displacement at points *Y* and *Z* and applied load. Test 45 with 1 geogrid and Test 22 with 2 geogrids. The top geogrid measures 180 mm, the second 110 mm

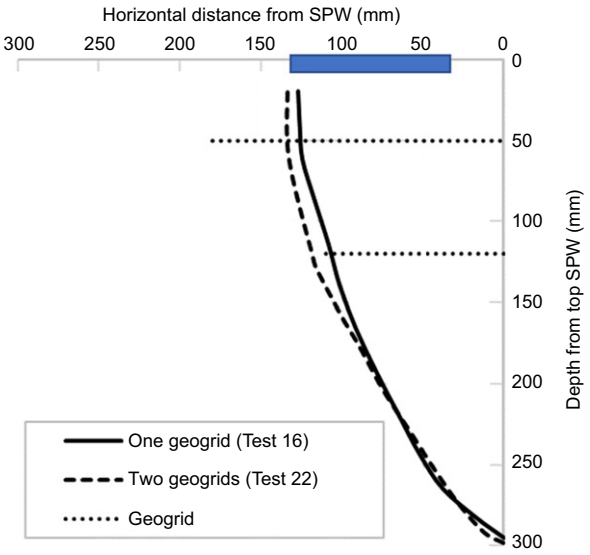

Figure 8. Effect of a second geogrid on the critical slip surface. The top geogrid measures 180 mm, the second 110 mm

by the rear part of the geogrid behind the critical slip zone (zone III) and the front part in zone I. Comparing the tests with the non-connected and connected 180 mm geogrids showed that the connection with the sheet pile wall activates the rear part in zone III but that the sliding soil mass in the active zone II dominates in the activation of the rear part at higher load levels.

A side note on the membrane effect: the mechanism in which the geogrid anchor is dragged down with the soil (in zone II), resulting in tensile forces in the geogrid, is referred to as the 'membrane effect'. This term refers to the capacity of the geogrid to be deformed, absorbing forces which were initially perpendicular to its surface. Due to a secondary effect, tensile forces develop in the geogrid through which the geogrid transfers vertical soil pressures to zone I, the SPW, if connected, and zone III.

Resistance in zones I and II is only mobilised when the geogrid is connected to the SPW or if the geogrid length is extended sufficiently into zone III. If the geogrid is dragged down with the soil, vertical soil pressures are transferred via the geogrid to the SPW and zone III.

3.6. Reproducibility

This section discusses the measured soil displacement and the observed critical slip surfaces for the test configurations with one 110 mm geogrid (Tests 12 and 13) or one 180 mm geogrid (Tests 16, 17 and 45). The load plate was 30 mm away from the SPW in both test configurations.

The reproducibility of the tests appears to depend to a major extent on the failure mode of the SPW. Reproducibility is high when the SPW fails by overturning (Figure 10b). This failure mode was observed for the test configurations with geogrids shorter than 130 mm. In the case of test configurations with a 180 mm geogrid, the geogrid provided so much resistance that the failure mode of the SPW changed from sliding and overturning to failure in which the SPW mainly slides along the bottom of the box (Figure 10a), with the SPW starting to slide at a higher surcharge level. This resulted in a higher frictional force along the bottom of the box, with a negative effect on reproducibility.

The more curved slip surface for geogrids with a length of 180 mm was discussed in Section 3.2. All three tests had this curved slip surface, as seen in Figure 11a. However, another, straighter, slip surface developed initially in only two of the three 180 mm tests. This straight slip surface matched the critical slip surface found in the tests with a short geogrid (≤130 mm) presented in Figure 11b.

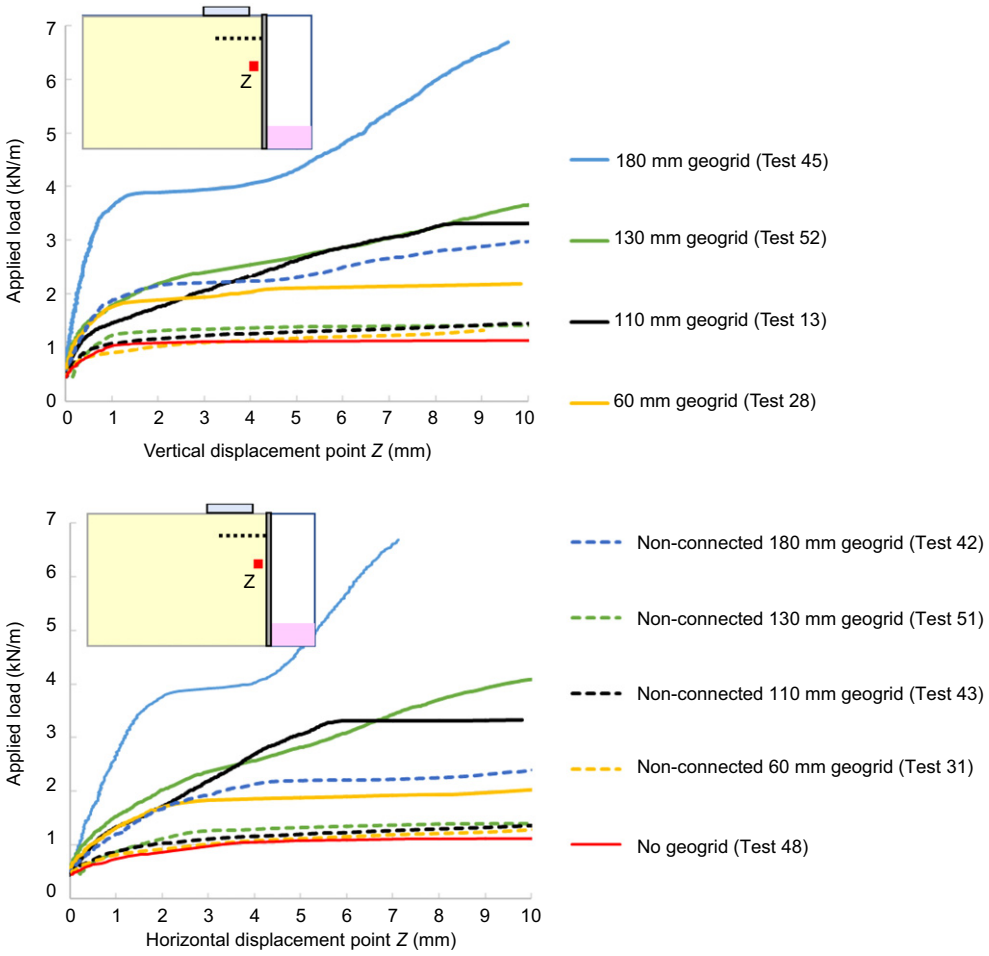

Figure 9. The difference between a connected and a non-connected geogrid, measurements at point *Z*

The tests seem to indicate a dependency on the strain rate (Figure 10): two 180 mm geogrid tests (Tests 16 and 17) with the same loading rate (0.021 and 0.020 kg/s) gave slipping at a similar load level. Test 45, however, with a different loading rate (0.033 kg/s) gave slipping at another load level. This finding contradicts the finding of Suescun-Florez *et al.* (2015) that strain rate effects for dry soil are negligible for confining pressures ≤100 kPa.

3.7. Influence of the width of the test box

3.7.1. *Description of additional tests in a wider test box*

Two additional tests were performed in a box that was eight times wider than the box used in the small-scale tests (785 mm instead of 100 mm) in order to determine whether the narrow box in the small-scale tests and the frictional force between the soil and the side walls affect the shape of the slip surfaces and the vertical load distribution. The additional tests differed in five ways from the tests described in Section 2:

- Side-wall friction was not reduced by lubricating and placing a silicone sheet against the side walls in order to improve the image quality. The sand was therefore in direct contact with the glass side walls.
- The distance between the SPW and the back wall increased from 415 mm to 724 mm. As in the small-scale tests, back-wall friction will not affect soil deformation.
- The passive side of the SPW was again simulated with a silicone block. However, the stiffness of the fabricated silicone block for this 785-mm-wide SPW turned out to be 1.5 times higher ($E = 245$ kPa) than the stiffness of the silicone block used in the small-scale test.
- The strip footing surcharge load was applied with a twin-piston hydraulic pressure system. The pistons were 44 mm in diameter and they were positioned 220 mm from the side walls. The vertical displacement of the loading plate was slowly increased with a hand pump. Figure 13 shows that the resulting loading rate fluctuated more than in the small-scale tests, in which the barrel was filled with a constant flow rate.
- The SPW was glued to the silicone block in such a way that there was a gap of 1 mm between the SPW and the bottom of the box. Reproducibility was therefore improved by reducing the friction between the SPW and the bottom of the test box.
- Total pressure cells (TPCs) were placed at the bottom of the box to measure the vertical soil pressures.

The test configuration with one 180 mm geogrid anchor and a surcharge load position 30 mm from the SPW was chosen. Tests 16, 17 and 45 were repeated in this wider test box.

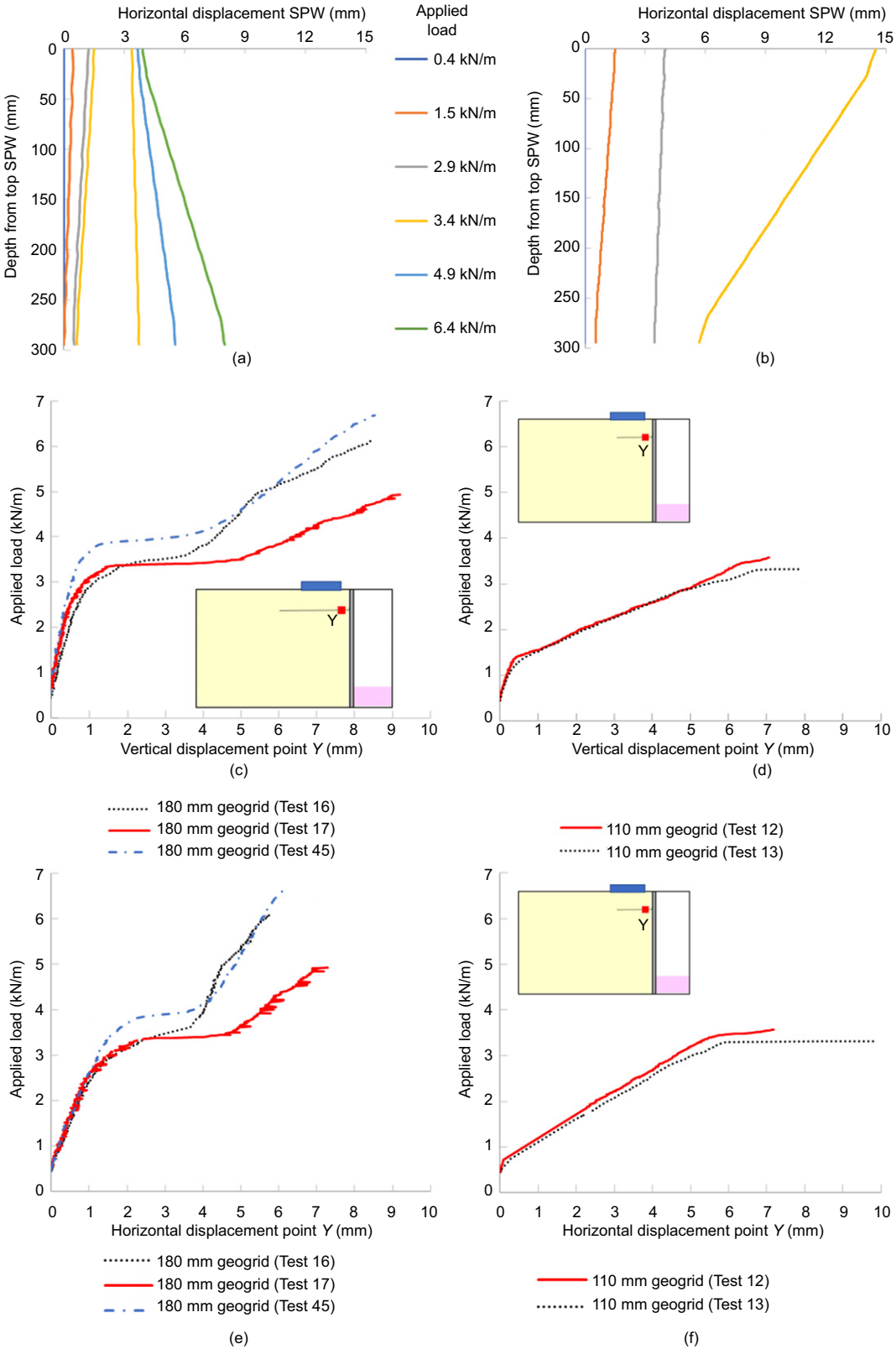

Figure 10. Measured displacement (top) of the sheet pile wall and (bottom) point *Y*. Tests with (left) one 180 mm geogrid and (right) one 110 mm geogrid

In the narrow test box in Section 3, wall friction was reduced by lubricating and placing a silicone sheet against the side walls. This was not done in the wider box. By looking at the stresses measured in the tests in the wide test box, Section 3.6.2 looks at whether the influence of side-wall friction in the wider box on the soil pressures is negligible and can be rightfully ignored. Section 3.6.3 then compares the slip surfaces that developed in the narrow and wide boxes.

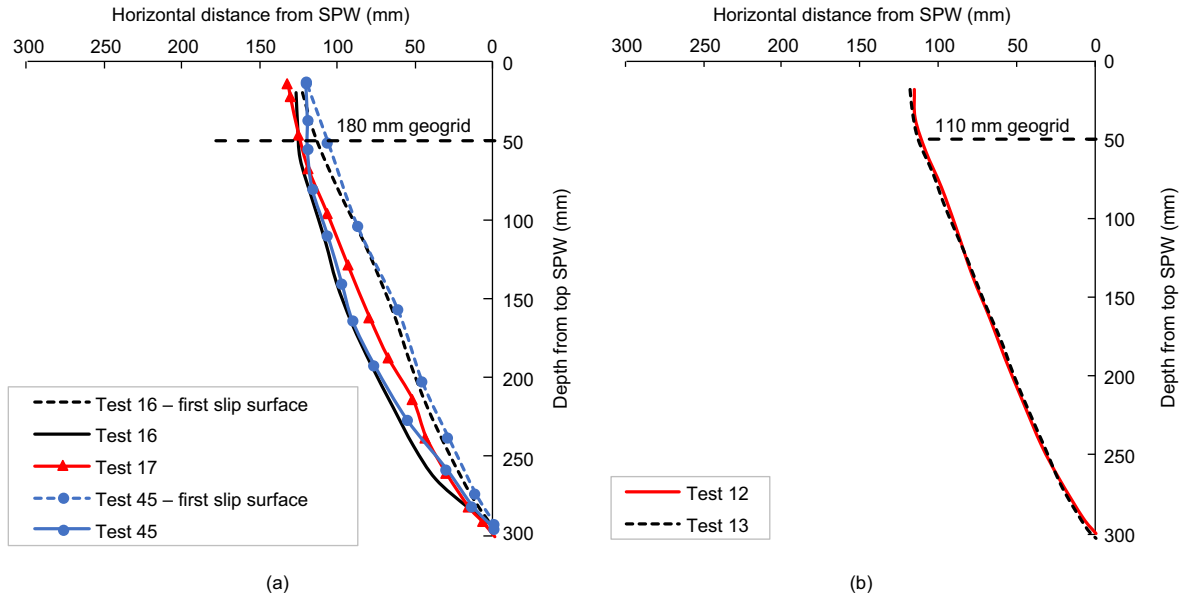

Figure 11. Observed initial and critical slip surfaces, tests with 1 geogrid; 180 or 110 mm

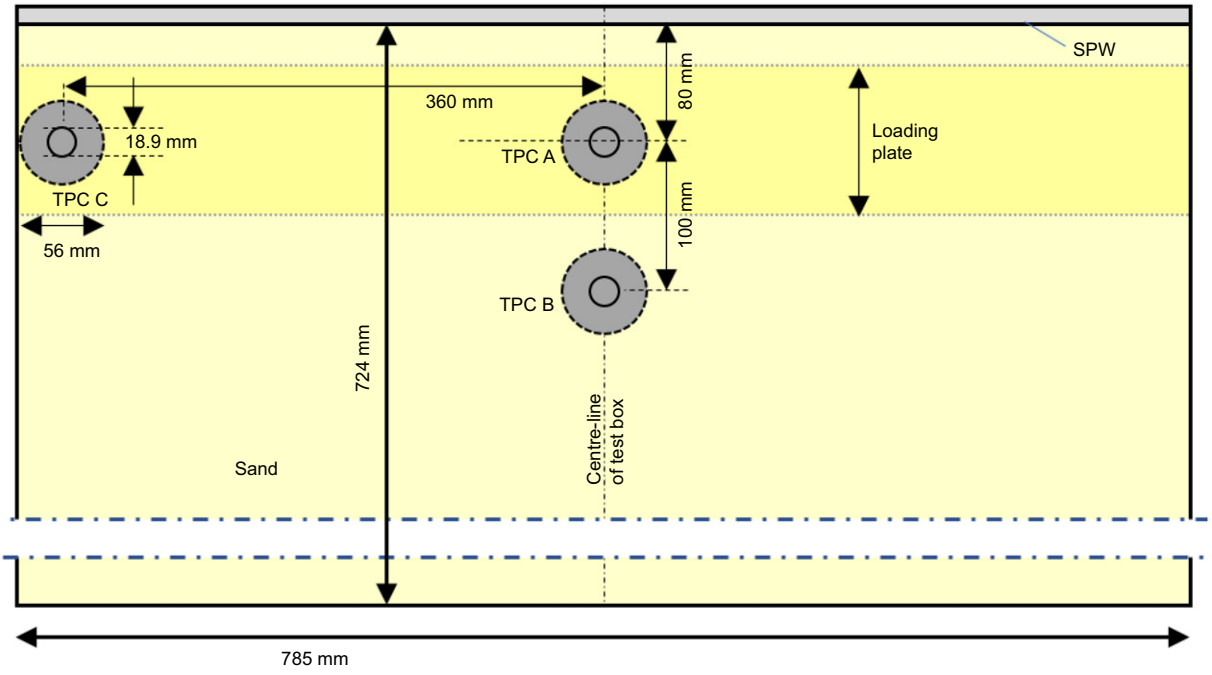

Figure 12. Top view of wider box used for Tests 5 and 6 showing the location of the three TPCs that were installed on the bottom of box

3.7.2. *Effect of side-wall friction on load distribution*

Three TPCs were placed in the bottom of the test box to measure the vertical pressure. Figure 12 shows the location of the TPCs.

Figures 13 and 14 show the vertical soil pressures measured by TPCs A, B and C. Figure 13 presents the surcharge load in kPa on the left axis and in force per unit metre SPW width (kN/m) on the right axis. The soil self-weight at the bottom of the box is approximately 4.7 kPa. This has been excluded in Figures 13 and 14 by setting the measured vertical soil pressures to zero at the start of the test.

The loading rates and measured vertical pressures in Tests 5 and 6 were very similar. The slip surfaces developed fully after five minutes. Interestingly, the measured vertical soil pressures at the bottom of the box were halved at the moment that the slip surface developed, indicating the activation of the geogrid anchor and a transfer of load to the SPW. Figure 14 shows that the vertical pressures in the centre of the test box and close to the side wall (TPC A and C respectively) were a reasonable match in Test 5. Although the values for TPC C were slightly higher than for TPC A in Test 6 between minutes 2 and 4, it can be concluded that the vertical pressure close

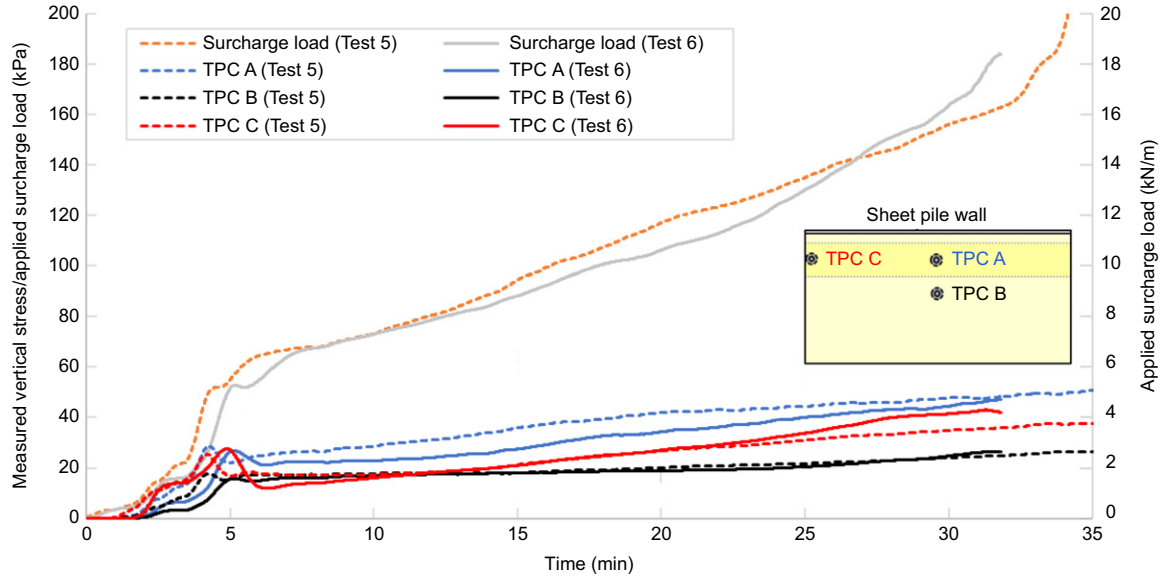

Figure 13. Tests 5 and 6: measured vertical soil pressures (TPCs A, B and C) at the bottom of the box and the applied strip footing surcharge and self-weight of the soil form the start to the end of the test. The measured soil pressures were set to zero before the surcharge load was applied

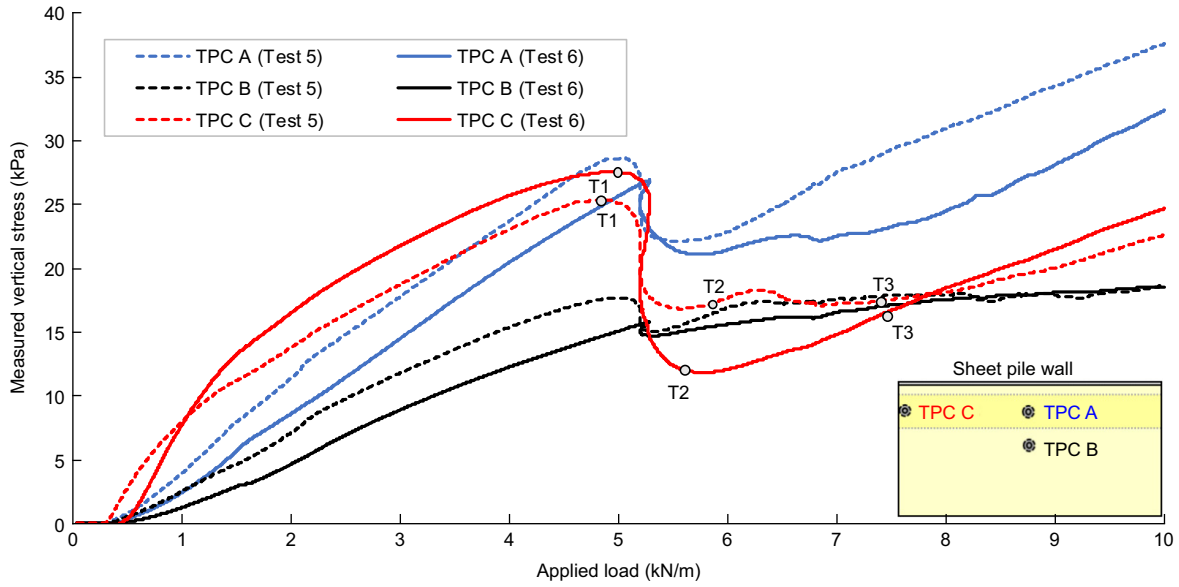

Figure 14. Tests 5 and 6: measured vertical soil pressures (TPCs A, B and C) at the bottom of the box and the applied strip footing surcharge load for surcharge load levels ≤10 kN/m. Three time stamps (T1, T2 and T3) are shown for which the shear strain soil response is plotted in Figures 15 and 16

to the side walls was not reduced by side-wall friction. On the basis of these measurements, it can be concluded that the load distribution and therefore the slip surfaces will not be affected by side-wall friction in this test set-up.

3.7.3. *Comparison of slip surfaces in the small-scale and wider test box*

Figures 15 and 16 show the slip surfaces in the tests with the wider test box tests at the three time points shown in Figure 14.

Figure 17 shows a comparison of the slip surfaces in the narrow and wide tests. A slip surface with a relatively wide curve developed in all these tests, not only in the narrow but also in the wider tests: the surfaces in the narrow and wider test boxes are a good match. These curved slip surfaces are the result of the presence of the geogrid: they are wider and more curved than the straight slip surface that would develop in circumstances without, or with short, geogrids. On the basis of Figure 17, then, we may conclude that the shape of the critical curved slip surface was not affected by the width of the test.

A straight slip surface sometimes developed before the wide slip surface or simultaneously with the wide slip surface. This was seen in both the small-scale and wide tests. Figure 17 shows this for Tests 5, 16 and 45. The

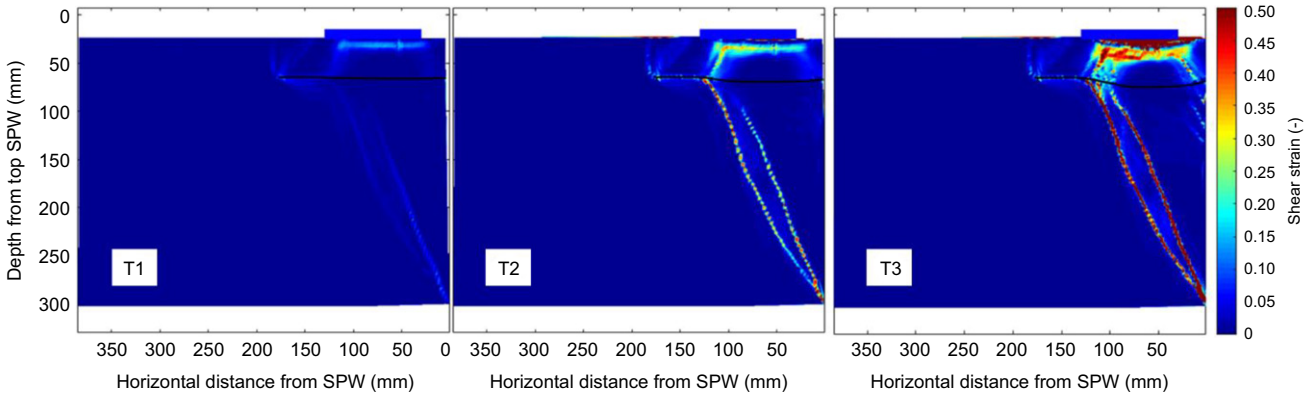

Figure 15. Shear strain in Test 5 at the three time points (T1, T2 and T3) shown in Figure 14. The initial position of the footing is denoted

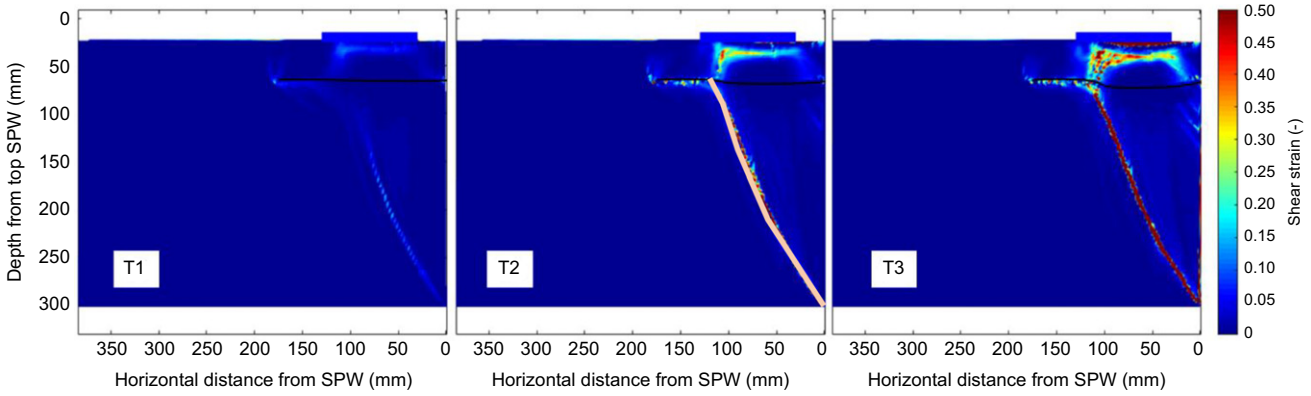

Figure 16. Shear strain in Test 6 at the three time points (T1, T2 and T3) shown in Figure 14. The initial position of the footing is denoted

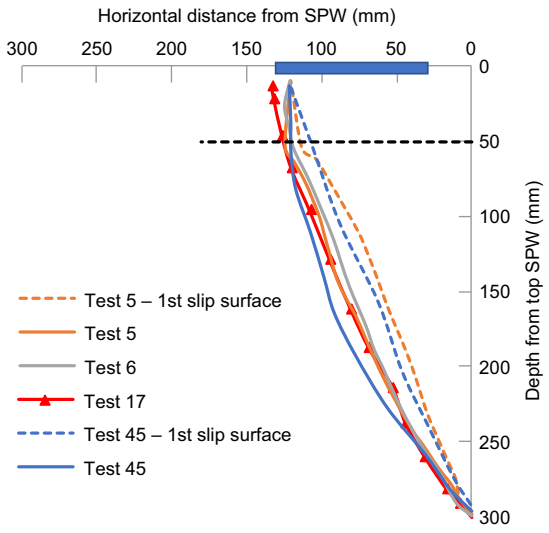

Figure 17. Comparison of slip surfaces in small-scale test box (Tests 17 and 45) and wider test box (Tests 5 and 6)

development of a straight slip surface may depend on minimal differences (<1 mm) in the test preparations such as the initial position of the SPW or slack in the geogrid.

Overall, the two tests in the wider box demonstrated the validity of the slip surfaces that developed in the small-scale test box.

4. NUMERICAL CALCULATIONS

4.1. Numerical model

The tests were simulated using a Plaxis 2D (version 2019) finite element model. The geometry is shown in Figure 18. The behaviour of the backfill was described with the Hardening Soil (HS) model, while a linear-elastic model described the silicone block behaviour on the passive side of the SPW. The SPW and load plate were modelled with plates. The geogrid was modelled as a 1D tensile element.

Tables 3 and 4 give the input parameters of all the materials. The bottom of the test box was included in the model to describe the friction of the SPW and silicone block along the bottom. Table 5 gives the parameters of the interfaces.

A dummy material was introduced to simulate the interaction between the sand and the geogrid. In the dummy material, the interface parameter R_{int} was kept to 1 (fully rough surface), while the internal friction angle of the sand (φ) was reduced to arctan (μ) at the interface, where μ is the apparent coefficient of friction. This parameter μ was determined on the basis of pull-out tests and a typical value is 0.8 for sands. In the dummy material, a reduction of 35% was applied to the dilatancy angle of the sand (ψ), in line with the reduced friction angle at the interface geogrid-soil.

- Simulating failure for non-associative models, as in the Hardening soil model, is notoriously difficult

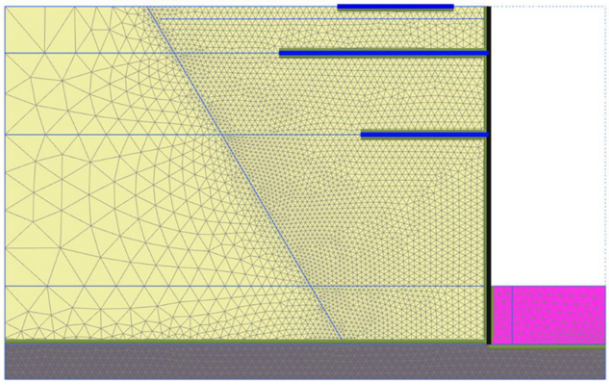

Figure 18. Build-up of numerical model in 8 phases

Table 3. Material properties in the numerical model of Baskarp B15 sand

Parameter	Symbol	Value
Unit weight (kN·m^{-3})	γ_{unsat}	16.3
Void ratio (–)	e_{init}, e_{min}, e_{max}	0.579, 0.385, 0.8
Secant Young's modulus (kN·m^{-2})	E_{50}^{ref} [a]	72.4×10^3
Oedometer stiffness (kN·m^{-2})	E_{oed}^{ref}	85.0×10^3
Unloading/reloading stiffness (kN·m^{-2})	E_{ur}^{ref}	443×10^3
Power (–)	m	0.54
Effective cohesion (kN·m^{-2})	c	0.6
Effective internal friction angle (°)	φ	45
Poisson ratio (unloading/reloading) (–)	ν_{ur}	0.2
Dilatancy angle (°)	ψ	16.5
Lateral earth soil pressure coefficient (–)	K_0^{NC}	0.5 [b]

[a]Reference pressure of 100 kPa.
[b]A relatively high value for K_0^{NC} was selected to account for the densification processes (tamping).

due to the localisation of large shear deformations. It was decided to model the soil with six node elements in order to make it possible to use more elements within a reasonable calculation time. This results in thinner slip surfaces and a calculation that runs more smoothly. The large differences around the slip surfaces will affect fewer elements if a larger number of smaller elements are used.

- Figure 18 shows the numerical model. During the preparation phase for the small-scale test, a stiff PVC plate was placed between the SPW and the front wall of the test box to restrain the lateral deformation of the SPW during preparation. The model simulated this by introducing a fixed-node anchor on the passive side of the sheet pile wall.
- The strip footing surcharge load was simulated by a prescribed displacement at the centre of the strip footing plate. A prescribed displacement was used instead of a prescribed load to prevent numerical problems.

Table 4. Material properties in the numerical model of the geogrid, SPW, loading plate and silicone block

Material	Parameter	Symbol	Value
SPW support	Axial stiffness (kN)	EA	5500
Geogrid	Axial stiffness (kN·m^{-1})	EA	191
SPW	Axial stiffness (kN·m^{-1})	EA	700×10^3
SPW	Bending stiffness (kNm^2·m^{-1})	EI	5.83
Loading plate	Axial stiffness (kN·m^{-1})	EA	73.5×10^3
Loading plate	Bending stiffness (kNm^2·m^{-1})	EI	5.6
Silicone block	Unit weight (kN·m^{-3})	γ_{unsat}	10.5
Silicone block	Void ratio (–)	e_{init}	0.5
Silicone block	Young's modulus (kN·m^{-2})	E	159
Silicone block	Poisson ratio (–)	ν	0.495

4.2. Results numerical calculations; parameter study

The numerical results are presented here for two test configurations: a test with one 180 mm geogrid anchor and a test with a second 110 mm geogrid anchor. The load was positioned 30 mm to 130 mm from the SPW in both tests. Section 6.1 analyses the effect of adding a second geogrid anchor by comparing the slip surface and axial force in the SPW. Section 6.2 analyses the tensile stress distribution and frictional forces along the geogrids of the SPW anchored with two geogrids.

4.2.1. *Anchors with one and two geogrids*

Figure 19a shows that the critical slip surface circumvents the bottom 110 mm geogrid and reorients perpendicularly to the initially horizontal top geogrid. This finding concurs with the test results of Ziegler (2010). Figure 19b shows an increase, at a surcharge load level of 3 kN/m, of 27% in the axial forces in the toe of the SPW when a second geogrid is added. This finding proves that the load transfer via the geogrid to the SPW contributes to the total stability of the SPW. The vertical soil pressures close to the SPW are reduced and therefore the horizontal pressures on the SPW.

4.2.2. *Mobilised tensile force and frictional forces along the geogrids*

Figure 20 shows the general failure mechanism calculated for two geogrids and the positioning of the strip footing 30 mm to 130 mm from the SPW. The grey lines represent the slip surfaces. The failure mode of the SPW is shown by the black arrows: the toe of the SPW slides along the bottom of the box while the top of the SPW moves less and therefore the SPW tilts backwards relative to the toe. The deformation of the geogrids is given for four different load levels. The figure shows that the top geogrid deforms like a hammock as the load level increases, while the rear part of the bottom geogrid is dragged down along with the soil.

Figure 21 shows the calculated tensile force distribution at different load levels in the top 180 mm geogrid anchor. The figure shows that the share of the mobilised tensile force of the geogrid between the secondary

Table 5. Material properties of the interfaces

Interfaces	Interface reduction coefficient[a] R_{int} (–)	Interface cohesion c_{int} (kPa)	Interface friction angle δ_{int} (°)	Interface dilatancy angle ψ_{int} (°)
Footing/sand	0.29	0.17	16.2	0
Geogrid/sand	1	0.6	38.7	10.7
SPW/sand	0.667	0.4	33.1	0
SPW/silicone block	0.5/1[b]	—	—	0
Sand/bottom box	0.29	0.17	16.2	0
SPW/bottom box	0.5	—	—	0
Silicone block/bottom box	0.5	—	—	0

[a]The final calculated displacements are very sensitive to the value of R_{int} that expresses the interaction between the SPW and the silicone block and the bottom of the test box. The value for R_{int} may range between 0.1 and 0.5. The stick-slip behaviour in the test implies variable friction forces which cannot be described by a constant interface coefficient.
[b]The numerical models of the tests in the small-scale test set-up all included an interface reduction coefficient between the SPW and the test box bottom of 0.5. The numerical model simulating Test 6 included an interface reduction coefficient of 1 (fully rough interface) since the SPW was glued to the silicone block. This parameter proved to have a negligible influence on the final load-displacement results for the SPW system.

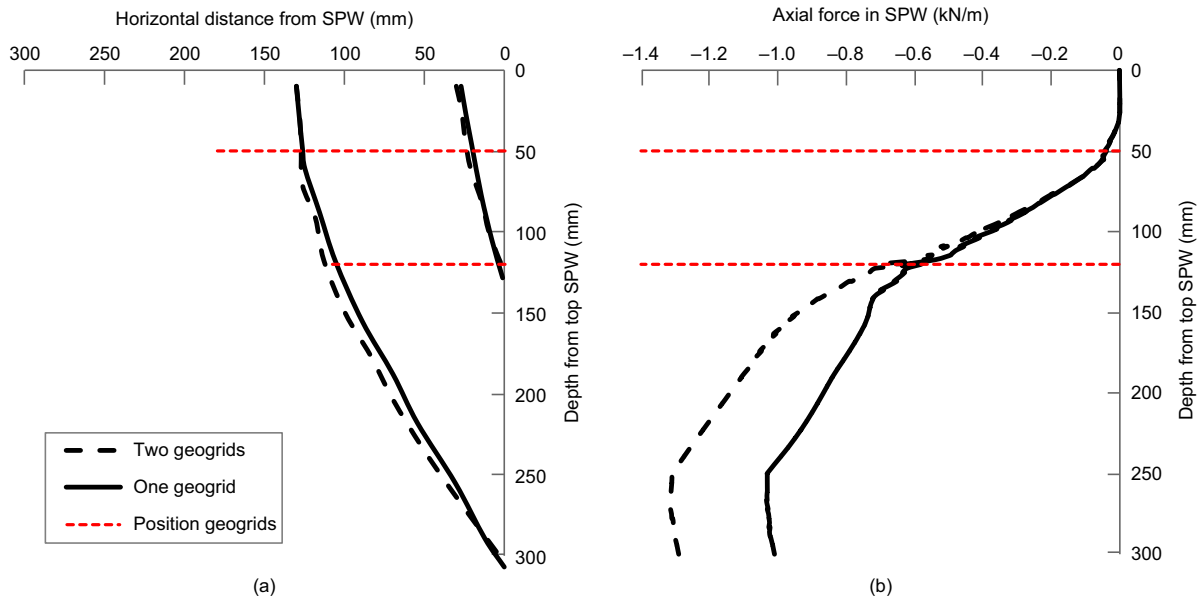

Figure 19. Numerical results comparing one 180 mm geogrid and two geogrids of 180 and 110 mm: (a) slip surfaces (b) axial force in the SPW at an applied load of 3 kN/m

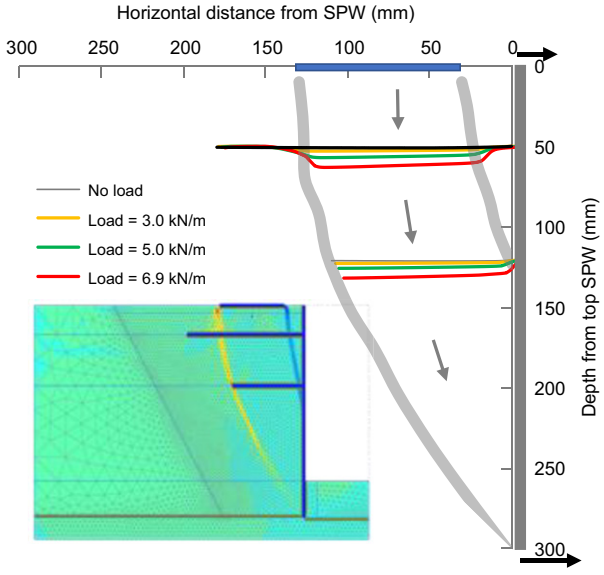

Figure 20. Numerical simulations of Tests 22 and 23: deformation of geogrids in test with two geogrids

curved slip surface and first straight slip surface rises continuously with increasing load level until an applied load of just above 5 kN/m. At that point, the critical slip surface has fully developed, and the geogrid is activated along a larger length of the geogrid between the secondary slip surface and critical slip surface (zone II, see Figure 3).

Figure 22 compares the mobilised tensile force in the geogrid and friction along the bottom and top interfaces of the 180 mm top geogrid (left) and 110 mm bottom geogrid (right). A general distribution of the frictional force along the top and bottom of the geogrids is presented in Figure 23.

Figures 22 and 23 show that, in the active zone (zone II), friction resistance is mainly mobilised along the bottom of the top geogrid. In zone III, however, friction is mobilised primarily along the top of that geogrid behind the critical slip surface. The shares of the friction along the top and bottom interfaces of the 18 cm geogrid are ~40% and ~60% of total resistance respectively.

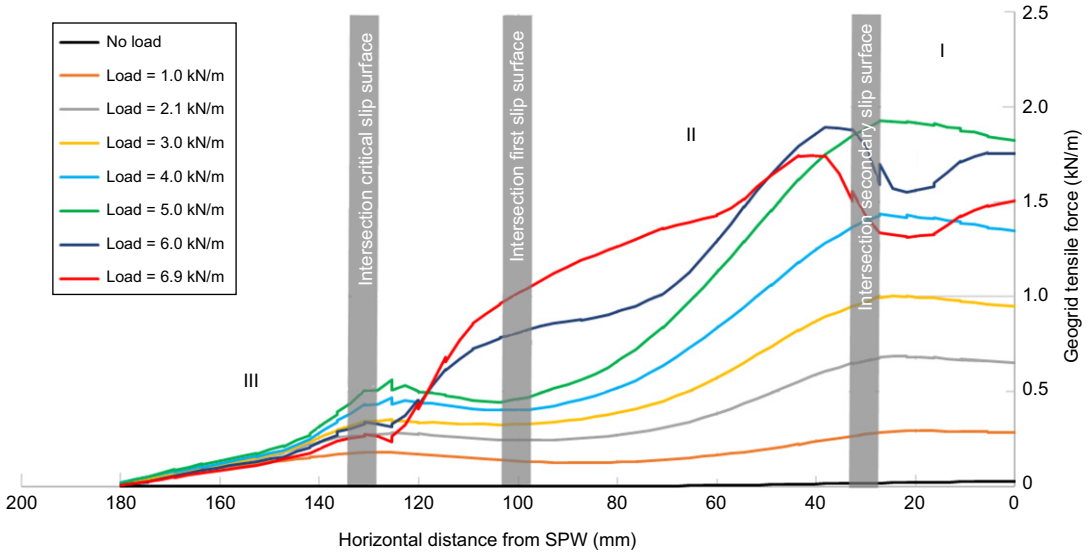

Figure 21. Numerical results: mobilised tensile force in 180 mm top geogrid at different surcharge load levels

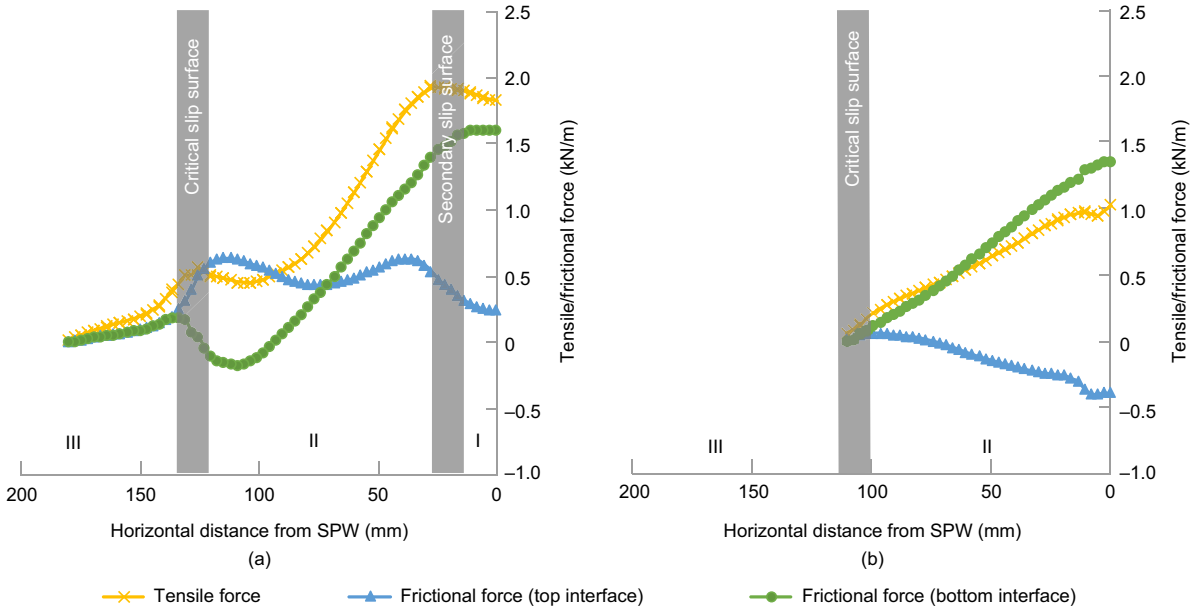

Figure 22. Numerical results: mobilised friction along (a) the top geogrid and (b) the bottom geogrid at an applied load of 5 kN/m

5. DISPLACEMENT; COMPARISON OF NUMERICAL AND EXPERIMENTAL RESULTS

5.1. Introduction

This section compares the experimentally and numerically determined deformations of the soil, the geogrid and the SPW respectively.

5.2. Soil deformation

The 2D numerical model was validated with Test 45 in the small-width test box and Tests 5 and 6 in the wider test box. These tests had one 180 mm geogrid anchor and the load plate was positioned 30 mm away from the SPW. As seen in Section 3.6, plane-strain conditions were met in the wide tests, Tests 5 and 6, and the wide tests produced similar slip surfaces to the small-scale tests. In Test 45, a silicone block that was less stiff was used at the passive side of the SPW so that the slip surfaces developed at a lower surcharge load and there was more deformation at the same applied load than in Tests 5 and 6.

Figures 24–27 compare the soil displacements, geogrid deformation and the horizontal displacement of the rear end of the geogrid and SPW displacement respectively.

The PIV results gave the soil deformation, but they were also used to retrieve the geogrid deformation by assuming equal displacement of the geogrid and the surrounding soil. This assumption results in large deviations between the actual geogrid deformation for the part of the geogrid which is being pulled out of the soil, in other words the rear part of the geogrid behind the slip surface. The deformation of the geogrid was therefore derived by

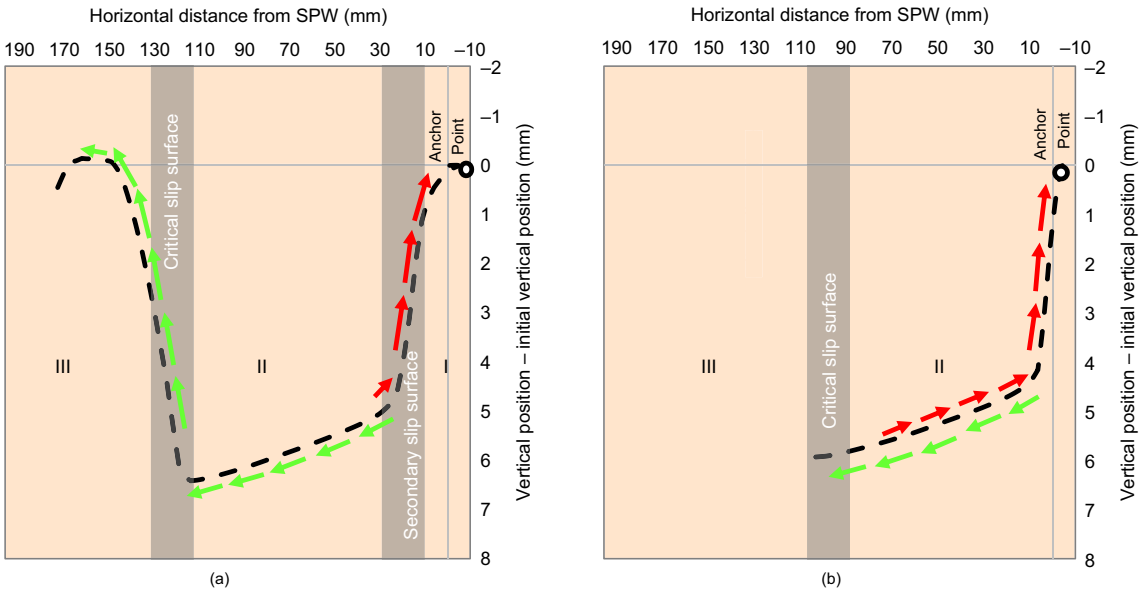

Figure 23. Numerical results showing parts of geogrid along which friction is primarily mobilised: (a) top geogrid (b) bottom geogrid

manually tracking the transversal ribs of the geogrid. Results were obtained from Tests 45 and 6 only: the geogrid could not be seen clearly on the photos from Test 5.

The slip surfaces in Tests 5 and 6 developed at a surcharge load level of approximately 5 kN/m (see Section 3.6). This already happened at 4 kN/m in Test 45. The development of the slip surfaces corresponds with large soil displacements at these load levels, and with the SPW becoming unstable. In both tests, this moment seems to occur slightly later in the numerical model. Before and after this moment of instability, the measured soil response is stiffer than in the calculations. The over-predicted soil displacement values can be ascribed in part to the stick-slip behaviour of the SPW and the silicone block, which is absent in the numerical model.

5.3. Geogrid deformation

The calculated maximum settlement of the geogrid is overestimated by ∼0.4 mm to ∼1.5 mm at the surcharge load levels indicated in Figure 25. The calculated part of the geogrid that is dragged down with the soil was wider than measured.

Figure 26 shows that the rear end of the geogrid was pulled out. For an applied load of 6 kN/m, the geogrid was pulled out by 7.6 mm in Test 45 and 4.0 mm in Test 6. The numerical model overpredicts the horizontal displacement of the rear end of the geogrid during the entire test by ≤2 mm. Nevertheless, the rates at which the geogrid was pulled out matched very closely.

5.4. SPW deformation

- Figure 27 shows the displacement of the SPW in Test 6 as determined by manually tracking the top and toe of the SPW in the test photos and the numerical model respectively. The toe of the SPW in the test lags behind at surcharge load levels ≤2.4 kN/m compared to the position calculated in the simulations. This may be clarified by the stick-slip mechanism of the SPW and the silicone block, which is absent in the numerical model. Nevertheless, the values for the magnitude of displacement are a reasonable match at surcharge load levels ≤5.3 kN/m. The deformation mode of the SPW can be described by translation in both the numerical model and the test. At surcharge load levels >5.3 kN/m, however, there were significant differences in the failure mode of the SPW. These results show that the resistance of the geogrid anchor must have been underpredicted. The overestimation of SPW deformation is in line with the overestimation of soil displacement for the larger surcharge load levels in Figure 24.
- The larger deformation values for the upper part of the SPW in the numerical model may indicate that the interface parameters between the soil and the geogrid must have been underpredicted.

6. COMPARISON WITH DESIGN GUIDELINES

Geogrid anchors may be a promising alternative for conventional anchors for SPWs, and for geosynthetic-reinforced retaining walls. This study with small-scale tests could represent a first step towards a design method for SPWs with this specific type of anchor.

- Both the numerical and test results show that the ‘effective length’ (the part behind the active zone) of anchors as defined by current design guidelines for SPWs (e.g. CUR166 2012) is conservative for geogrid anchors for SPWs subjected to a strip footing load. Subject to confirmation in full-stress situations, consideration could be given to taking the mobilised friction of the part of the geogrid in the active zone into account in order to reduce the required length of

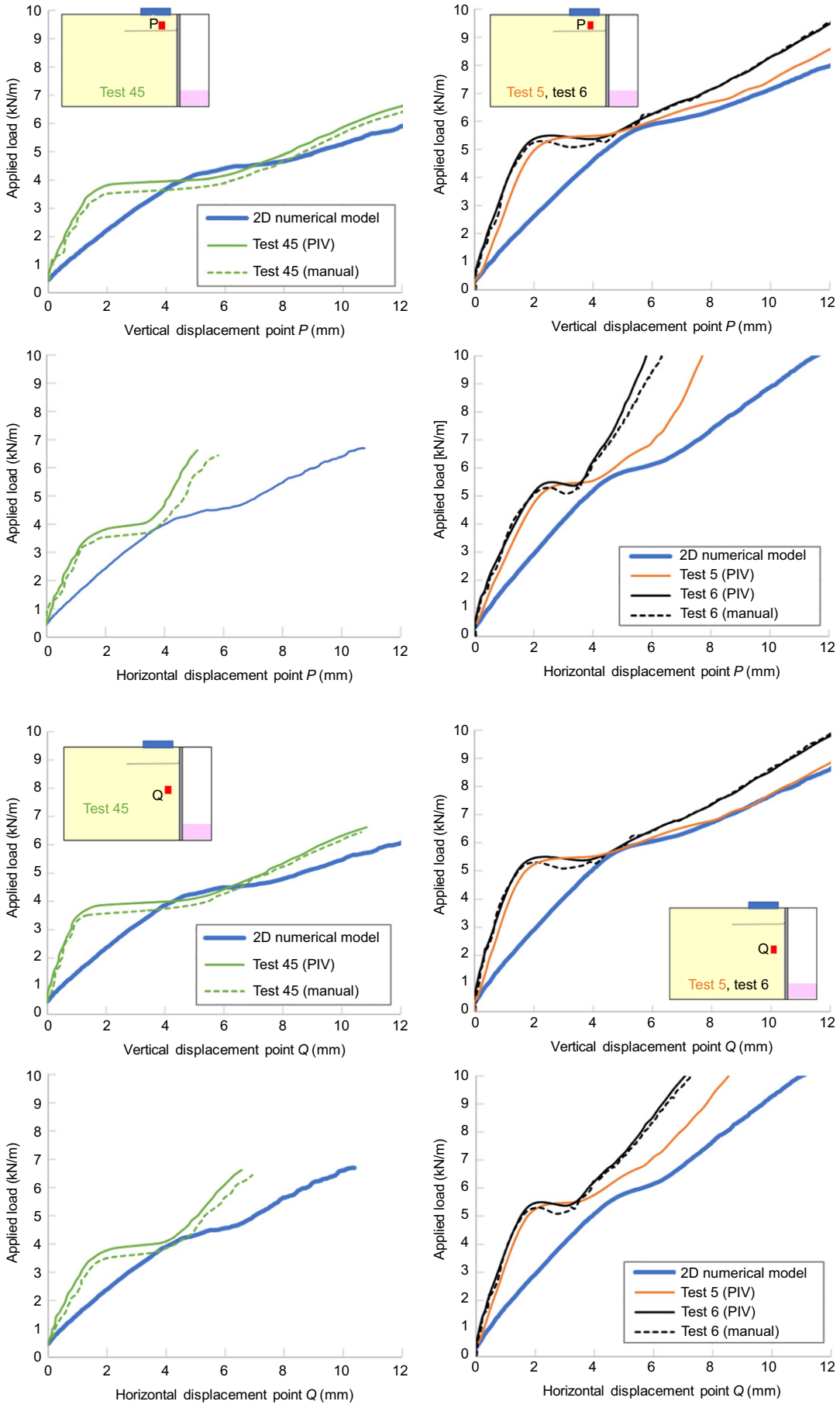

Figure 24. Comparison of numerical and test results, soil displacement at points *P* and *Q*

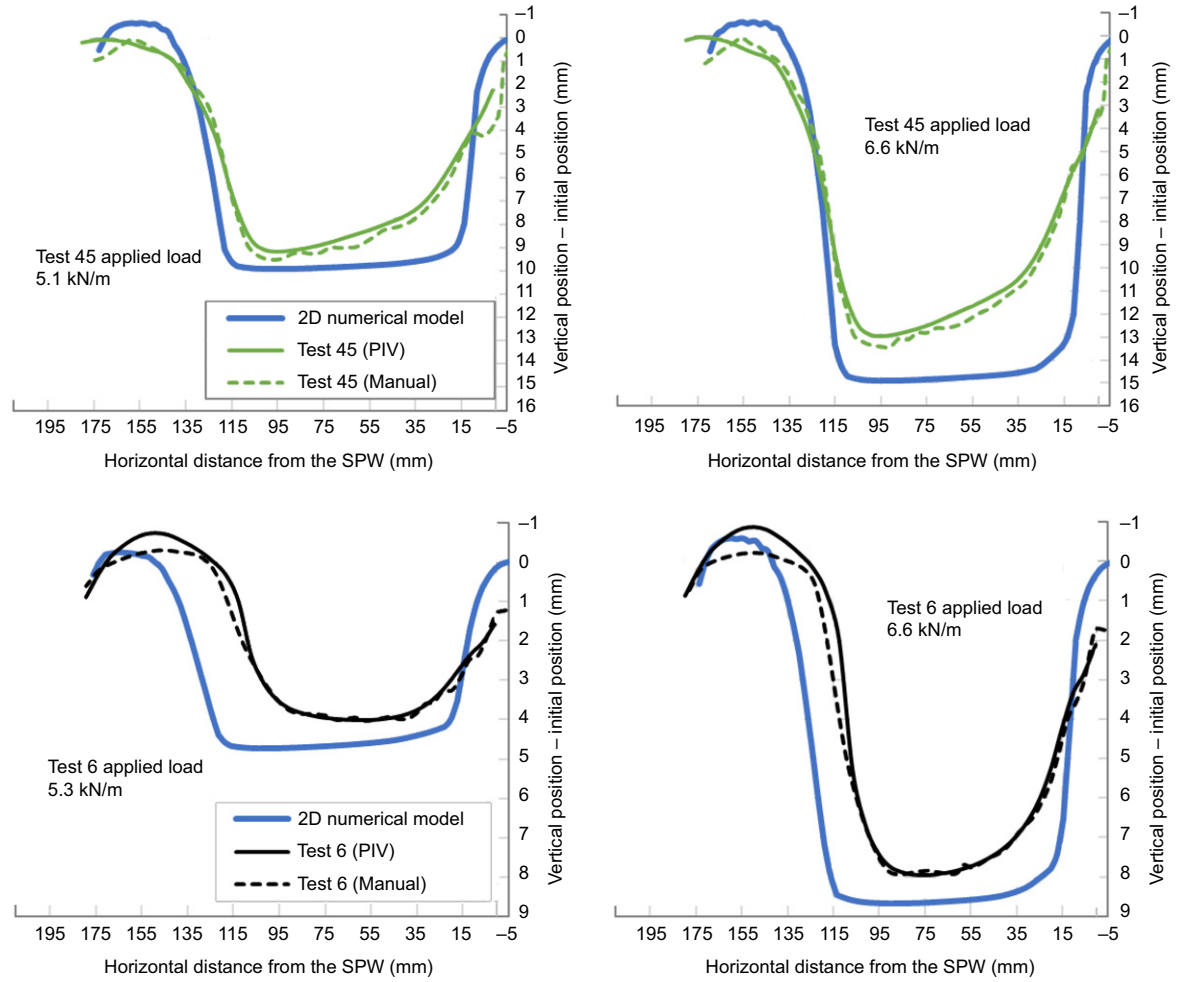

Figure 25. Comparison of numerical and test results; deformed geogrid. The horizontal and vertical axes have different scales

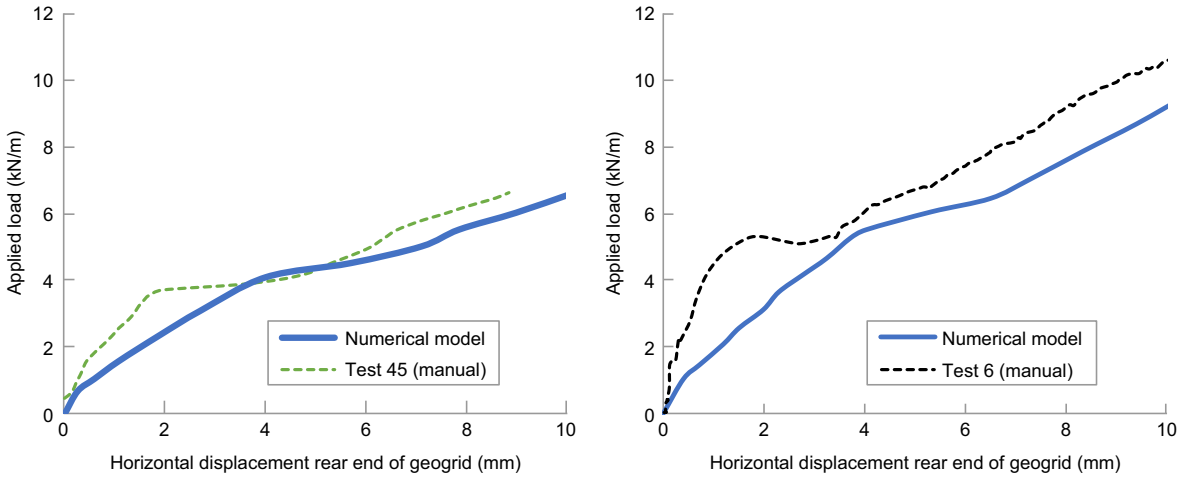

Figure 26. Comparison of numerical and test results; horizontal displacement of the rear end of the geogrid

geogrid anchorages for situations with strip footing loading.

- The contribution of the geogrid-soil friction in the active zone is triggered by settlement, which occurs if the soil is excavated on the passive side or if a surcharge load such as a strip footing load is exerted on the active side. Unlike conventional anchors, the geogrid anchor provides a stabilising effect when the slip surface intersects with the geogrid, in which case the geogrid changes the shape of the slip surface. This effect should be included in the design of geogrid-anchored SPWs.

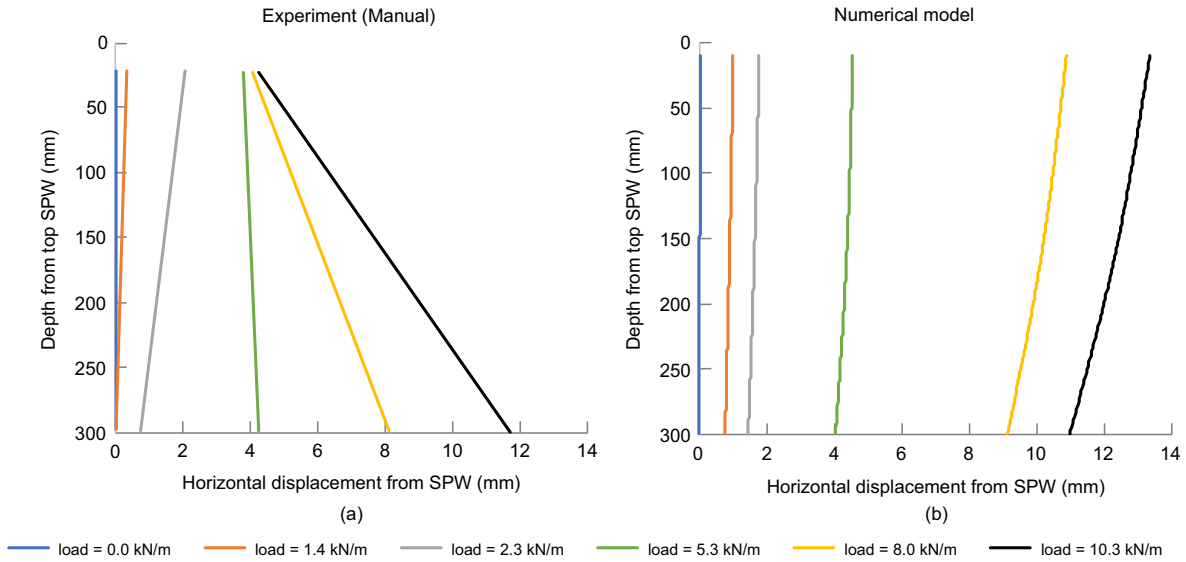

Figure 27. SPW displacement at different surcharge load levels: (a) measured in Test 6 (b) calculated

- The membrane effect is expected to reduce the vertical soil pressures close to the SPW, and therefore the horizontal pressures on the SPW. Accordingly, the required stiffness of the SPW or anchor forces may be reduced. Furthermore, it is important to examine the end bearing capacity of the SPW for the larger axial forces due to the larger transfer of the vertical soil pressures to the SPW.
- The numerical results showed that soil-geogrid friction was mobilised along either the top or the bottom of the geogrid only. This finding confirms the current Dutch design guideline for reinforced soils (CUR198 2017), in which the effective length of the geogrid is taken into account only once.

7. CONCLUSIONS

This paper presents the results and analyses of 1 g small-scale tests on geogrid-anchored SPWs subjected to a strip footing surcharge load. The results were simulated with a 2D numerical model. The following conclusions can be drawn from the tests:

- The failure mechanism generally consists of two slip surfaces that divide the soil into three different strain zones (I, II and III). These strain zones determine along which parts of the geogrid friction is mobilised.
- Zone I is the zone of rigid soil body motion between the wall and secondary slip surface, zone II is an active zone enclosed by the secondary slip surface and the critical slip surface and zone III is the stable soil zone behind the critical slip surface.
- The position and width of the strip footing load define where the slip surfaces develop at the ground surface level: at the inner or outer edge of the footing. The position of the strip footing with respect to the geogrids and the width of the strip footing therefore has a major effect on the mobilisation of friction along the geogrid. This is in line with the findings of Ahmadi (2020).
- Resistance in zones I and II is only mobilised when the geogrid is connected to the SPW or if the geogrid length is extended sufficiently into zone III. If the geogrid is dragged down with the soil, vertical soil pressures are transferred via the geogrid to the SPW and zone III.
- The resistance mobilised in zone III is described by pull-out mechanisms: the geogrid is pulled out of the soil either by the SPW or the sliding soil mass in the active zone.
- As expected, the length of the geogrid affects the mobilised resistance along the geogrid. The longer the geogrid, the more resistance is mobilised along the geogrid. In particular, a longer length behind the critical slip surface (zone III) increases the overall stability. A longer geogrid induced stiffer behaviour from the outset of our tests.
- The slip surface reorients vertically at the intersection of the critical slip surface with the geogrids, as was also found by Ziegler (2010) for reinforced soil. The resulting slightly wider and curved slip surfaces increase the soil shear resistance and the overall stability accordingly.
- Adding a short, second, geogrid anchor, in other words with the rear end in the active zone, reduces the deformation at larger load levels but the contribution to the overall stability is limited.

The tests in the wider test box, which include an SPW with one 180 mm geogrid anchor, were used to validate the numerical model. The resistance offered by the geogrid was underpredicted, resulting in values for SPW deformation at the top of the SPW that were too high. Soil displacement – in particular horizontal soil displacement – and geogrid deformation are therefore overpredicted as well. Nevertheless, the numerical results can be used qualitatively and they provide a good picture

of the mobilised tensile forces in the geogrid and frictional forces along the geogrid.

The following conclusions can be drawn from this numerical analysis:

- Soil along the bottom of the geogrid provides resistance in the active zone II.
- Soil along the top of the geogrid provides resistance in zone III, behind the active zone.
- No resistance is provided by the soil enclosed between the SPW and the secondary slip surface (zone I).

ACKNOWLEDGMENTS

The authors are grateful for the financial and practical support of the TKI-PPS funding of the Dutch Ministry of Economic Affairs, Deltares, Delft University of Technology, GeoTec Solutions, GMB Haven & Industrie, Huesker BV, Huesker GmbH, Ruhr-Universität Bochum Germany and Voets Gewapende Grondconstructies.

NOTATION

Basic SI units are given in parentheses.

B	width (m)
c	cohesion (Pa)
c_{int}	interface cohesion (Pa)
D_{50}	median particle diameter (m)
E	Young's modulus (Pa)
E_{50}	secant Young's modulus (Pa)
E_{50}^{ref}	secant Young's modulus at confining pressure of 100 kPa (Pa)
$E_{\text{oed}}^{\text{ref}}$	oedometer stiffness at confining pressure of 100 kPa (Pa)
$E_{\text{ur}}^{\text{ref}}$	unloading/reloading stiffness (Pa)
EA	axial stiffness (N)
EI	bending stiffness ($\text{Nm}^2\cdot\text{m}^{-1}$)
D_{60}/D_{10}	coefficient of uniformity (dimensionless)
e_{init}	initial void ratio (dimensionless)
e_{max}	maximum void ratio (dimensionless)
e_{min}	minimum void ratio (dimensionless)
$\boldsymbol{g}$	gravitational acceleration ($\text{m}\cdot\text{s}^{-2}$)
H	height (m)
I_{D}	relative density (dimensionless)
K_0^{NC}	lateral earth soil pressure coefficient (dimensionless)
L	length (m)
m	power in power law material stiffness (dimensionless)
N	geometrical scaling factor (dimensionless)
R_{int}	interface parameter (dimensionless)
γ_{unsat}	unsaturated unit weight ($\text{N}\cdot\text{m}^{-3}$)
δ_{int}	interface friction angle (°)
μ	apparent coefficient of friction (dimensionless)
ν	Poisson ratio (dimensionless)
ν_{ur}	Poisson ratio during unloading/reloading (dimensionless)
σ_3	minor principle stress ($\text{N}\cdot\text{m}^{-2}$)
$\sigma_{3,\text{ref}}$	minor principle stress at reference level of 100 kPa (Pa)
$\varphi_{\text{res}}^{\text{triax}}$	residual internal friction angle as derived from a triaxial test (°)
$\varphi_{\text{sec}}^{\text{triax}}$	secant internal friction angle as derived from a triaxial test (°)
ψ_{int}	interface dilatancy angle (°)
ψ^{triax}	dilatancy angle as derived from a triaxial test (°)

ABBREVIATIONS

1D	one-dimensional
2D	two-dimensional
HS model	hardening soil model
MSE	mechanically stabilized earth (walls)
PIV	particle image velocimetry
PVC	polyvinylchloride
SPW	sheet pile wall
TPCs	total pressure cells
US	United States

REFERENCES

Ahmadi, H. (2020). *Geosynthetic-Reinforced Soil Retaining Walls Subjected to Surcharge Loads.* PhD Dissertation, Ghent University, Ghent, Belgium. ISBN: 978-94-6355-342-1.

Ahmadi, A. & Hajialilue-Bonab, M. (2012). Experimental and analytical investigations on bearing capacity of strip footing in reinforced sand backfill and flexible retaining wall. *Acta Geotechnica*, **7**, No. 4, 357–373, https://doi.org/10.1007/s11440-012-0165-8.

Bathurst, R. J. & Benjamin, D. J. (1987). Preliminary assessment of sidewall friction on large scale wall models in the RMC test facility. In *The Application of Polymeric Reinforcement in Soil Retaining Structures.* Jarret, P.M.P. and McGown, A., Editors, Kluwer Academic Publishers in cooperation with NATO Scientific Affairs Division, Dordrecht, The Netherlands, pp. 181–192.

Bathurst, R. J. & Naftchali, F. M. (2021). Geosynthetic reinforcement stiffness for analytical and numerical modelling of reinforced soil structures. *Geotextiles and Geomembranes*, **49**, No. 4, 921–940.

Bathurst, R. J., Miyata, Y., Nernheim, A. & Allen, A. M. (2008). Refinement of K-stiffness method for geosynthetic-reinforced soil walls. *Geosynthetics International*, **15**, No. 4, 269–295, https://doi.org/10.1680/gein.2008.15.4.269.

BSI (2010). BS8006-1: Code of practice for strengthened/reinforced soils and other fills. BSI, London, UK.

CUR166 (2012). *Damwandconstructies (Dutch Design Guideline Sheet Pile Walls), Including errata 2014*. CROW, Gouda, Netherlands, ISBN: 9037600638.

CUR198 (2017). *Ontwerprichtlijn Kerende Constructies van Gewapende Grond (Dutch Design Guideline Soil Retaining Constructions of Reinforced Soil)*. CROW, Delft, Netherlands, ISBN: 9789053676509.

Detert, O., Lavasan, A., van den Berg, J., van Duijnen, P., König, J. D., Hölter, R. & van Eekelen, S. J. M. (2019). Geogrid-verankerde damwanden. Deel 1: voorbeeldprojecten en onderzoeksopzet. (Geogrid-anchored sheet pile walls. Part 1: example projects and research program). *Geokunst, Geotechniek*, **November 2019**, 60–64, in Dutch.

Dijkstra, J., Broere, W., Bezuijen, A. & van Tol, A. F. (2008). Density changes near an advancing displacement pile in sand. In *The*

Proceedings of: The Second British Geotechnical Association International Conference on Foundations (ICOF 2008), Brown, B. J., Bransby, M. F., Brennan, A. J. & Knappett, J. A., Editors, IHS Bree Press, Berkshire, UK, pp. 545–554.

DIN EN ISO (2015). 10319:2015-09: Geosynthetics – Wide-Width tensile tests. ISO 10319:2015, Beuth, Germany.

EBGEO (2010). *Empfehlungen für den Entwurf und die Berechnung von Erdkörpern mit Bewehrungen aus Geokunststoffen – EBGEO*. German Geotechnical Society, Berlin, Germany, vol. 2, ISBN: 978-3-433-02950-3. Also available in English: Recommendations for Design and Analysis for Earth Structures using Geosynthetic Reinforcements (2011), ISBN: 978-3-433-02983-1.

Henkel, D. & Gilbert, G. (1952). The effect of the rubber membrane on the measured triaxial compression strength of clay samples. *Géotechnique*, **3**, No. 1, 20–29, https://doi.org/10.1680/geot.1952.3.1.20.

Iai, S. (1989). Similitude for shaking table tests on soil-structure-fluid model in 1-g gravitational field. *Soils and Foundations*, **29**, No. 11, 105–118.

Jayasree, P. K., Rajagopal, K. & Gnanendran, C. T. (2012). Influence of sidewall friction on the results of small-scale laboratory model tests: numerical assessment. *International Journal of Geomechanics*, **12**, No. 2, 119–126, https://doi.org/10.1061/(ASCE)GM.1943-5622.0000120.

Jewell, R. A. (1987). Analysis and predicted behaivour for the Royal Military College trial wall. In *The Application of Polymeric Reinforcement in Soil Retaining Structures*. Jarret, P.M. and McGown, A., Editors, NATO ASI Series (Series E: Applied Sciences). Springer, Dordrecht, Netherlands, vol. 147, pp. 193–238, https://doi.org/10.1007/978-94-009-1405-6_7. Kluwer Academic Publishers in cooperation with NATO Scientific Affairs Division, Dordrecht, Netherlands.

Lees, A. (2014). Measurement of the geogrid confining effect. *Paper Number 259. In Proceedings of 10ICG, September 2014*, Berlin, Germany, Ziegler, M., Bräu, G., Heerten, G. & Laackmann, K., Editors, Deutsche Gesellschaft für Geotechnik e.V.

PLAXIS 2D (2019). *Reference Manual Edition V20. Delft: Plaxis bv*. See https://www.plaxis.com/support/manuals/plaxis-2d-manuals/ (accessed 27/09/2022).

Rui, R., van Tol, A. F., Xia, Y. Y., van Eekelen, S. J. M. & Hu, G. (2016). Investigation of soil-arching development in dense sand by 2D model tests. *Geotechnical Testing Journal*, **39**, No. 3, 415–430, https://doi.org/10.1520/GTJ20150130. ISSN: 0149-6115.

Schaefer, V. R., Berg, R. R., Collin, J. G., Christopher, B. R., DiMaggio, J. A., Filz, G. M., Bruce, D. A. & Ayala, D. (2017). *Ground Improvement Methods – Reference Manual Vols. I and II*. FHWA-NHI-16-027 and FHWA-NHI-16-028. U.S. Department of Transportation Federal Highway Administration, Washington, DC. USA

Spingher, S. (2018). *Modellvalidierung Einer mit Geogittern Rückverankerten Arbeitsplattform zum Bau von Offshore-Windenergieanlagen*. MSc thesis, Ruhr-Universität Bochum, Bochum, Germany.

Stanier, S. A., Take, A., Blaber, J. & White, D. (2015). *GeoPIV-RG*. University of Western Australia, Queens' University, Canada. See http://www.geopivrg.com/ (accessed 27/09/2022).

Stanier, S. A., Dijkstra, J., Leśniewska, D., Hambleton, J. & White, D. (2016a). Vermiculate artefacts in image analysis of granular materials. *Computers and Geotechnics*, **72**, 100–113, https://doi.org/10.1016/j.compgeo.2015.11.013.

Stanier, S. A., Blaber, J., Take, W. A. & White, D. J. (2016b). Improved image-based deformation measurement for geotechnical applications. *Canadian Geotechnical Journal*, **53**, No. 5, 727–739, https://doi.org/10.1139/cgj-2015-0253.

Suescun-Florez, E., Iskander, M. & Bless, S. (2015). A model to predict strain rate dependency of dry silica sand in triaxial compression. *Journal of Dynamic Behaviour of Materials*, **1**, 447–461, https://doi.org/10.1007/s40870-015-0039-x.

Teng, Y., Stanier, S. A. & Gourvenec, S. M. (2017). Synchronised multi-scale image analysis of soil deformations. *International Journal of Physical Modelling in Geotechnics*, **17**, No. 1, 53–71, https://doi.org/10.1680/jphmg.15.00058.

van Duijnen, P. G., Detert, O., Lavasan, A. A., van den Berg, J., Hölter, R., König, D. & van Eekelen, S. J. M. (2022). Geogrid-anchored sheet pile walls: field test and numerical analyses. *Published in the Proceedings of the 7th European Geosynthetics Conference (EuroGeo7)*, Warsaw, Poland, pp. 108–118.

Wittekoek, B. (2020). *Analysis of the Behaviour of Geogrid-Anchored Sheet Pile Walls. Small-Scale Experiments and 2D Plaxis Analysis*. MSc thesis, Delft University of Technology, Delft, Netherlands. See https://repository.tudelft.nl/islandora/object/uuid%3A94cf64cc-ff09-4fbe-bde8-42d914b3c7d0.

Yang, K. H. & Liu, C. N. (2007). Finite element analysis of earth pressures for narrow retaining walls. *Journal of GeoEngineering*, **2**, No. 2, 43–52.

Ziegler, M. (2010). *Investigation of the Confining Effect of Geogrid Reinforced Soil with Plane Strain Model Wall Tests*. Rheinische Westfälische Technische Hochschule Aachen, Aachen, Germany.

The Editor welcomes discussion on all papers published in Geosynthetics International. Please email your contribution to discussion@geosynthetics-international.com